A Numerical Investigation of Self-Excited Combustion Instability

Mechanical engineering

Intelligent structures and mechanics system engineering

Tokushima University

Nannan Dang

Supervisor： Prof. Yoshihiro Deguchi

september 2021

ABSTRACT

Nowadays, combustion provides more than 80% of the worldwide energy sources. However, practical combustion systems are often susceptible to combustion instabilities characterized by large-amplitude and low-frequency pressure oscillations. This dissertation presents a nonlinear analysis and a Computational Fluid Dynamics (CFD) simulation of those self-excited combustion instabilities with a Rijke tube combustor. It is necessary to learn the mechanisms of combustion instabilities in-depth to prevent combustion instabilities or control them at acceptable levels.

The nonlinear analysis of the combustion is implemented first. A model of a one-dimensional (1D) Rijke tube burner with both ends opened is built. The nondimensional momentum equation and energy equation of the acoustic perturbation are derived and solved in the time domain by using the Galerkin technique. A saturated n-τ model is proposed to descript the nonlinear flame heat release rate. The time evolution of the combustion instability is calculated. The stabilities of the systems under given conditions are determined by calculating the eigenvalues. Next, the bifurcation analysis of the dynamics behavior for the Rijke burner is performed for the variation of flame location, flame heat release intensity, and the time lag between heat release and flow velocity perturbation. Nonlinear phenomena, including hysterical, critical bifurcation, and stability switching, were observed, verifying the nonlinear characteristic of the Rijke tube burner. Further, the phase diagram and Poincaré map of the limit cycle oscillations are given, showing the oscillations' periodic character. The growth rates of the onset for the exciting case and decay for the stable case are calculated too. This nonlinear analytical method helps to understand the nature of combustion instability.

Second, the self-excited combustion instability in a two-dimensional (2D) Rijke tube burner with a center-stabilized premixed methane-air flame is numerically studied. The simulation considers the reacting flow, flame dynamics, and radiation model to investigate the essential physical processes. A finite volume-based approach is used to

simulate reacting flows. Chemical reaction modeling is conducted via the species transport model with one-step reaction mechanisms, and the radiation heat flux is determined by using the P-1 model. The steady-state reacting flow is first simulated for model verification. Then, the dynamic pressure, velocity, and reaction heat evolutions are determined to show the onset and growth rate of self-excited instability in the burner. The growth rates of the acoustic disturbances at the onset stages are calculated by curve fitting. Using the fast Fourier transform (FFT) method, the limit cycle oscillation frequency is obtained, which agrees well with the theoretical prediction. The dynamic pressure and velocity along the tube axis provide the acoustic oscillation mode and amplitude, agreeing well with the prediction. Finally, the unsteady flow field at different times in a limit cycle shows that flame-induced vortices occur inside the combustor. The temperature distribution indicates that the back-and-forth velocity changes in the tube vary the distance between the flame and honeycomb in turn, forming a forward feedback loop in the tube. The results reveal the route of flame-induced thermoacoustic instability and indicate periodical vortex formation and breakdown in the Rijke burner.

In summary, the combustion instability in a Rijke type burner is numerically investigated from the nonlinear dynamics analysis and CFD simulation. The nonlinear analysis results show that combustion instability is a nonlinear system. There are bifurcation, stability switching phenomenons that exist, and the systems may have stable and unstable results for a given state. The CFD results verify the predictions of 1D analytical results and reveal details of the dynamics flow field, showing that even in very low Reynold numbers, the coupling of flow perturbation and heat release may induce vortices. These results provide people new perspective in studying the mechanisms of combustion.

KEYWORDS: Combustion instability, Nonlinear dynamics, Bifurcation analysis, CFD, Rijke burner, Stability switch, flame induced vortices.

TYPE OF THESIS: Combustion instability

Contents

1. Introduction

1.1. Combustion instability

Combustion is the primary source of the worldwide energy supply. The efficient and safe operation of combustion facilities has excellent economic value. However, practical combustion systems often face high-amplitude pressure oscillations that arise due to the interaction between unsteady heat release of the flame and flow disturbance in the overall system, as shown in Figure 1-1. These combustion instabilities (also called 'thermoacoustic instability') may induce unwanted structural vibration, efficiency decrease, loud noises, and even severe damages to the combustion devices.

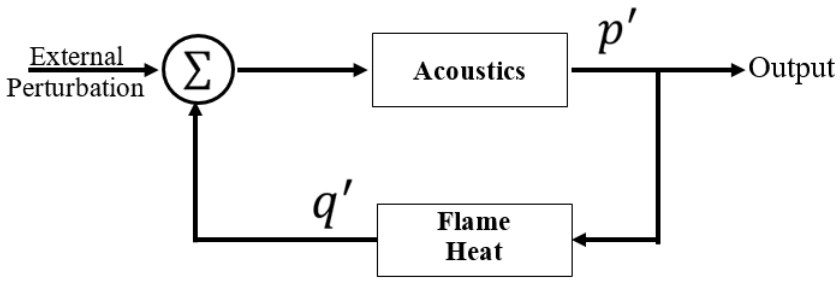

Figure 1-1 Combustion system with unsteady heat release

Another problem associated with combustion instability is the low-pollutant lean flame. In recent years, strict emission standards have been imposed on the design and manufacture of lean, premixed gas turbine combustors, requiring significant pollutant emission reduction, especially NO_x. The NO_x emission indeed decreases in lean flames, compared with the fuel-rich combustion. However, the flames tend to be unstable near the lean limit, and its coupling with acoustics may lead to combustion instability, causing flame out. Thus, the research on the mechanism of such combustion instability and the suppression methods have been a direction that many researchers have focused on.

To prevent these unwanted combustion instabilities or control them at acceptable levels, it needs to understand mechanisms and develop capabilities to predict the occurrence conditions. However, the development of combustion devices has shown that

thermoacoustic instability is rarely predicted reliably by tests and analysis [1]. There are three main reasons for this: first, thermoacoustic systems are time-delay systems, depending strongly on the time lag between heat release rate and pressure oscillations; second, thermoacoustic systems evolve interactions between reaction mechanisms, heat conduction, hydrodynamic and acoustic, which have different spatial and temporal scales and are sensitive to parameters; third, thermoacoustic systems contain elaborate nonlinear behaviors, such as periodic, quasi-periodic, frequency-locked, and chaotic behaviors [2]. For these reasons, the accurate modeling and thorough understanding of combustion instability remain challenging.

1.2. Rijke burner

Combustion instability is a complicated phenomenon. Some simplified models must be applied to understand its' nature. Various devices have been adopted to study combustion instability. In 1859, Rijke presented experimental results showing that when a heater was placed in a vertical tube, the expected steady natural convection was sometimes supplemented with acoustic oscillations [3]. The device illustrating this thermoacoustic phenomenon is called a Rijke tube. The Rijke tube, which is convenient for study both experimentally and theoretically, provides an elementary model of thermoacoustic oscillations due to the unsteady heat release and flow perturbations inside the tube. Because of this advantage, the Rijke tube has been extensively applied in thermoacoustic instability research, and its structure has been varied to several types [4]-[5]. Among these devices, one type in which the flow is a combustible gas, and the heat is produced by the flame is called a Rijke burner or a Rijke tube burner. Therefore, by researching the Rijke burner, it will be possible to discern the detailed information of the combustion instability that can be generalized to any combustor system.

1.3. Previous research of Rijke burner

Experimental research on the Rijke burner is intuitive and can yield highly reliable information about thermoacoustic instability, such as temperature, pressure, and

velocity. Abundant nonlinear behaviors, such as limit cycle oscillation, quasi-periodic, frequency-locked, and chaotic behaviors, were discovered [6]-[7]. Based on experimental results, some classical flame models have been proposed [8]-[12]. However, experimental methods can collect data only at finite points. They cannot obtain the entire field's parameters, and a comprehensive understanding of the flow field of thermoacoustic instability is still lacking.

Analytical studies have been conducted to explain the mechanisms of thermoacoustic instability since the 1960s [13]-[14]. Lord Rayleigh deduced the classical Rayleigh criterion to explain the mechanism of thermoacoustic instability [15]. Culick established the linear theory of combustion instabilities and first derived the nonlinear acoustic model in combustion chambers based on experimental research [16]-[19]. Balasubramanian and Sujith investigated the role of nonnormality and nonlinearity in flame-acoustic interactions and found that nonnormality and nonlinearity lead to triggering and redistribution of energy between eigenmodes [20]. Yoon et al. predicted the bootstrapping instability mechanism observed in rocket motors by approximated modal analysis [21]-[22]. Li et al. observed the stability switch phenomenon with a one-dimensional (1-D) Rijke-type thermoacoustic system [23]. Researchers have obtained a thoughtful understanding of the mechanism of thermoacoustic instability through the analytical method, especially for predicting the frequency, amplitude, and stability of self-excited thermoacoustic instability.

Since thermoacoustic instability often happens in a short time, it can develop from a steady state to a fully developed oscillation state at a millisecond-second time scale. Thus it is difficult to capture enough data on the occurrence and growth of this step, but with CFD simulation, the time step can be as small as 10^{-6} s; thus, this approach can yield deep insight into the detailed process of the occurrence and growth of instability.

Because of the nonlinearity in the combustion system, the interactions between reaction mechanisms, hydrodynamics, and acoustics reveal different spatial and temporal scales

and are sensitive to various parameters, resulting in obstacles in the accurate simulation of combustion instabilities. Nevertheless, with the development of computational technology, CFD simulations have increasingly helped to discern the mechanisms of thermoacoustic instability and to provide guidance for experimental research, making up for the shortage of experimental work.

Many numerical studies have been conducted on combustion instabilities. Wang successfully simulated the lean premixed combustion instabilities in a 2-D Rijke type burner and found that the radiation and reaction mechanism play critical roles in predicting the occurrence of thermoacoustic instability [24]. Chatterjee investigated the occurrence of combustion instabilities in a Rijke tube-type combustor using a 2D finite volume method, captured the instability growth to a limit cycle of the pressure oscillation, and predicted the frequency and magnitude of the thermoacoustic instability [25]. Chatterjee et al. also simulated a three-dimensional (3D) premixed chamber with ANSYS FLUENT software and studied the dependence of a homogeneous mixture on various parameters such as the premixing length, airflow rate, and equivalence ratio to optimize the combustor [26]. Blanchard et al. simulated a bluff-body flame holder, and the proper orthogonal decomposition modes of the simulated results and experiments showed quantitative agreement [27]. Ghulam et al. used COMSOL software to investigate the driving mechanism of combustion instabilities in a small rectangular combustion duct and obtained the pressure waves in the longitudinal and transverse directions [28]. On the research of the interaction of turbulence and combustion, numerical simulation has also shown its extraordinary ability [29]. These CFD simulations help in understanding the detailed flow parameters, such as pollution control, efficiency enhancement, and mass transport processes for further analysis and can thus serve as an aid to engineers and designers for building combustion systems with a decreased possibility of thermoacoustic instabilities.

1.4. Outline of thesis

With the development of combustion facilities, combustion instabilities are widely arising in modern industrial systems. The high-amplitude and low-frequency pressure oscillations during combustion instability are of significant damage to the system and hard to predict. Thus, the learning and control of combustion instability become an essential research topic. Previous researches on combustion instabilities have got actual results in learning the mechanisms of it; however, there are still some unsettled problems. The objective of this work is to investigate the nonlinear interaction of the unsteady heat release of premixed combustion and the acoustic field with nonlinear dynamics theory. The main work contains two parts: the first is the nonlinear analysis of a 1D model, and the second part is a CFD simulation of the 2D Rijke burner.

1) The nonlinear analysis of combustion instability.

The governing equation of the acoustic perturbations in the 1D Rijke burner is derived and projected to a finite-dimensional function space which is constituted by the natural acoustic modes of the burner. A saturated flame model is proposed based on the $n-\tau$ model. The equation is then solved using a Matlab program. The bifurcation plot, phase diagram and Poincaré map are drawn to analyze the nonlinear character of the combustion instability.

2) The CFD simulation of combustion instability.

The dynamic flow field of combustion instability in a Rijke burner is simulated in a 2D domain. The time evolutions of pressure, velocity, and combustion heat release are recorded. The growth rate of the instability, oscillating mode, and oscillating frequency are calculated. Finally, the evolution of flow field and streamline in an oscillating cycle are given, revealing the coupling among flow, combustion, and acoustic field.

2. Nonlinear analysis of the combustion instability

2.1. Nonlinear theory of combustion instability

From 1963 to 1983, Rott published a series of articles and established the classical linear thermoacoustic theory, which theoretically clarified the mutual transformation of heat and work in the thermoacoustic effect and laid the foundation for the modern linear thermoacoustic theory[30]-[35]. At present, the linear theory becomes the most effective and widely used theory in thermoacoustic research.

The Rayleigh criterion and linear theory can help to predict frequencies and growth rates of linearly unstable modes. However, they can neither predict oscillation amplitudes nor a system's susceptibility to being triggered by finite-amplitude excitations. Besides, many experiments have revealed that even simple thermoacoustic systems exhibit nonlinear behavior like triggering, saturation, frequency-switching, and chaos. Experiments also show that higher frequency modes, which are linearly stable, become significant through nonlinear growth. Thus, using nonlinear analysis methods to investigate the complicated nonlinear phenomena in combustion instability is of great importance, especially for predicting frequencies, amplitudes, and stability of self-excited combustion instability.

In 1990, Heckl [36] studied the nonlinear effect in the Rijke tube theoretically and experimentally. He pointed out that the nonlinear effect in the Rijke tube is mainly caused by flow reversal at the heat source and nonlinear effects at the ends of the tube. The former has a noticeable effect when the magnitude of the velocity disturbance and the mainstream velocity is equal, resulting in the decrease in heat transfer rate, and is the crucial reason for the limitation of the oscillation amplitude; the latter highlights the effect of increasing the loss of the nozzle when the pressure oscillation amplitude is high, but the effect is relatively small. By studying the nonlinearity of the thermoacoustic interaction of the Rijke tube and the nonlinear radiated acoustic resistance at the end of the tube, Han Fei et al. [37]-[38] proposed that the role of the

nonlinear effect is to limit the increase in amplitude and stimulate the output of high-order harmonics. In 2003, Matveev [39] concluded in his doctoral dissertation that in a large number of systems, the nonlinear acoustic loss caused by sound intensity is not large enough to become the main reason for the nonlinear saturation of thermoacoustic oscillation. Balasubramanian and Subramanian et al. [40], [41] first proposed the non-orthogonal phenomenon in the Rijke tube and concluded that non-orthogonality could lead to amplitude saturation even in the absence of damping through numerical simulation. Ma Dayou [42] conducted a systematic study on thermoacoustic oscillation and deduced the detailed, rigorous solution according to the Rayleigh criterion, giving the corresponding solution of nonlinear traveling wave and standing wave in the tube. Yoon et al. [22] used the Rijke rocket engine as the object and described the bootstrapping phenomenon in the evolution of nonlinear velocity-sensitive thermoacoustic instability system, as follows, the first mode initially decays and then grows, the energy of the first mode is first transferred to the second mode, stimulating the amplitude of the second mode to increase, while the amplitude of the first-order mode decreases; then the second mode transfers energy to the first mode, leading to the increase of the amplitude of the first-order mode also. Li Guoneng et al. [43] studied the Rijke-type premixed burner with an open end and a closed end and found that the frequency of pulsation hopped from one resonance to another during the start-oscillation of thermoacoustic insatiability in the Rijke burner. That is, lower resonances were first triggered and then damped quickly, then higher resonances were re-triggered, so on and so forth, until suitable resonances were reached. Huang X et al. [44] summarized the research progress of Rijke-type thermoacoustic self-excited oscillation and pointed out that there is no theory that can fully explain the mechanism of thermoacoustic oscillation. The existing theories are only applicable to weak nonlinearities and should be self-excited in the tube. Further research should be carried out on nonlinear phenomena and the establishment of nonlinear models. In 2014, Sayadi et al. [45] pointed out in their research that when the heat release rate is low, the primary

oscillation frequency of the system is the unstable mode after linearization. However, when the heat release rate increases to a certain extent, the system will excite other high-order frequencies, but in linear analysis, these frequencies may be stable. Kashinath [46] coupled the combustion G equation and the acoustic wave equation and obtained two ways for Rijke thermoacoustic oscillation to lead to chaos: period-doubling bifurcation and Ruelle-Takens-Newhouse path. It was found that flame wrinkles and pinch-off are the origins of periodic sound waves. In 2017, Li et al. [23] studied the effects of time lag, acoustic loss, and combustion-flow coupling on the stability of Rijke tubes. The heat source was selected as the n-τ model proposed by Fleifil et al. [10] in 1990, and they found the delay-independent region where changing the time delay will not affect the stability of the system, and stability switches region where a continuous increase of the time delay can lead the stability switches between stability and instability. Nevertheless, this article is based on a linear model, and only the first mode is selected, so the result should actually be a linear result.

The objective of this chapter is to investigate the effect of the average heat release intensity, flame location, and the time delay between unsteady heat release and velocity perturbation in the Rijke burner on the dynamics characteristics. The stability character of a 1D Rijke type combustion system is studied numerically. First, the nondimensional governing equations of the acoustic perturbation are derived from N-S equations. The heat souse of this Rijke burner is a premixed flame and its' heat release rate is described by a saturated n-τ model. Then the governing equations are solved by using the Galerkin method with a self-programed Matlab Procedure. The results show that there are Hopf bifurcations when varying the intensity of average heat release, and supercritical bifurcation when varying the flame location, and the system stability changes with time delay periodically, these results can help understand the nonlinear character of the combustion instability.

2.2. Physical and mathematical models

2.2.1. Rijke model

The Rijke tube model is a one-dimensional horizontal tube with a flame burner confined with it, as shown in Figure 2-1. Both ends are acoustically opened boundaries. The length of the tube is L, and the flame is located at $\tilde{x}_f$.

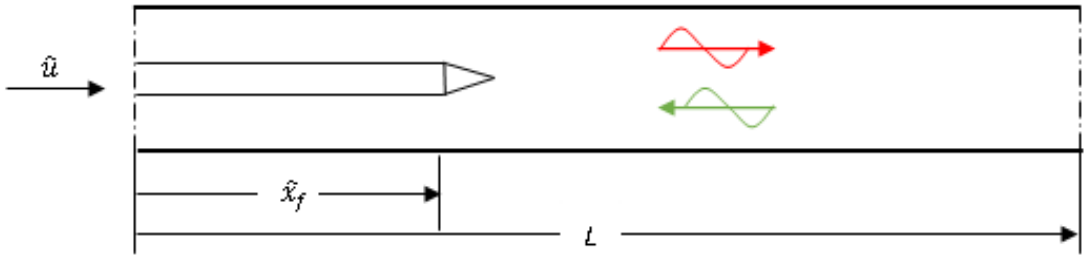

Figure 2-1 Schematic of the 1-D Rijke-type burner

The governing equation of the model starts from the N-S equations. Assuming that the combustible gas feed into the tube is an inviscid nonconducting ideal gas, and its heat conduction and viscosity are ignored. Since the temperature range and pressure range of the air in the Rijke tube are between 240 K <T <2000 K, p < 9.8×10^5 Pa, therefore, the complete gas equation of state can be used, the constant pressure specific heat capacity c_p and the constant volume specific heat capacity c_v are constant, Eq. (2-1) is obtained as the governing equations.

$$\begin{cases} \dfrac{\partial \tilde{\rho}}{\partial \tilde{t}} + \tilde{\rho}\dfrac{\partial \tilde{u}}{\partial \tilde{x}} + \tilde{u}\dfrac{\partial \tilde{\rho}}{\partial \tilde{x}} = 0 \\ \tilde{\rho}\left(\dfrac{\partial \tilde{u}}{\partial \tilde{t}} + \tilde{u}\dfrac{\partial \tilde{u}}{\partial \tilde{x}}\right) + \dfrac{\partial \tilde{p}}{\partial \tilde{x}} = 0 \\ \dfrac{\partial \tilde{p}}{\partial \tilde{t}} + \tilde{u}\dfrac{\partial \tilde{p}}{\partial \tilde{x}} + \gamma\tilde{p}\dfrac{\partial \tilde{u}}{\partial \tilde{x}} = (\gamma-1)\tilde{Q}\delta(\tilde{x}-\tilde{x}_f) \\ \tilde{p} = \tilde{\rho}R\tilde{T} \end{cases} \tag{2-1}$$

where $\tilde{x}$ and $\tilde{t}$ are the position and time, respectively, and $\tilde{\rho}$, $\tilde{p}$, $\tilde{u}$ and $\tilde{Q}$ are the density, pressure, velocity, and total heat released from the flame, respectively. $\tilde{T}$ is the temperature, $R = c_p - c_v$ is the gas constant, δ is the standard Dirac function.

Define the dimensionless quantities as follows:

$$\tilde{x} = Lx \qquad \tilde{t} = \frac{L}{a_0}t \qquad \tilde{u} = u_0(1+u') \qquad \tilde{p} = p_0(1+\gamma MP')$$

$$\tilde{\rho} = \rho_0(1+\rho') \qquad a_0 = \sqrt{\gamma \frac{p_0}{\rho_0}} \qquad M = \frac{u_0}{a_0} \qquad \tilde{Q} = Q_0(1+Q') \tag{2-2}$$

where x and t are the nondimensional position and time, respectively, a is the sound speed, M is the Mach number, and the subscript '0' and superscript ‘’ denote the average and perturbation quantities, respectively. Since the velocity and velocity disturbance terms are relatively small relative to the speed of sound, therefore, in the derivation process, both the velocity and velocity disturbance terms are ignored.

Hence, the nondimensional acoustic equation can be written as

$$\begin{cases} \dfrac{\partial u'}{\partial t} + \dfrac{\partial p'}{\partial x} = 0 \\ \dfrac{\partial p'}{\partial t} + \dfrac{\partial u'}{\partial x} = \dfrac{(\gamma-1)\mathrm{Q}_0}{\gamma u_0 p_0} Q'\delta(x-x_f) \end{cases} \tag{2-3}$$

By introducing the velocity potential ϕ, which is defined as

$$u' = \frac{\partial \phi}{\partial x} \quad \text{and} \quad p' = -\frac{\partial \phi}{\partial t}. \tag{2-4}$$

the wave equation can be expressed as

$$\frac{\partial^2 \phi}{\partial t^2} - \frac{\partial^2 \phi}{\partial x^2} + \frac{(\gamma-1)\mathrm{Q}_0}{\gamma u_0 p_0} Q'\delta(x-x_f) = 0. \tag{2-5}$$

2.2.2. The damping model

Introducing acoustic damping ξ into equation (2-5), the damped wave equation can be written as

$$\frac{\partial^2 \phi}{\partial t^2} + \xi\frac{\partial \phi}{\partial t} - \frac{\partial^2 \phi}{\partial x^2} + \frac{(\gamma-1)\mathrm{Q}_0}{\gamma u_0 p_0} Q'\delta(x-x_f) = 0 \tag{2-6}$$

The damping loss of the Rijke tube thermoacoustic system is mainly caused by two parts, which are the boundary layer loss and the sound energy radiation loss at the end of the nozzle. Howe had proposed a damping model in the following form [47]:

$$\xi = \sum_{n=1}^{\infty} \xi_n \qquad \xi_n = \frac{1}{\pi}\frac{\omega_n^2 S}{La} + \frac{1}{\sqrt{2}}\frac{\Pi\sqrt{\omega}}{S}\left(\sqrt{\nu} + (\gamma - 1)\sqrt{\chi}\right) \tag{2-7}$$

where $\omega_n = \frac{\pi n a}{L}$ is the natural frequency of the n^{th} mode of the tube, ξ_n is the n^{th} damping coefficient, S and Π are the area and perimeter of the cross section of the burner, respectively, and ν is the kinematic viscosity.

In simplified form, ξ_n can be written as

$$\xi_n = c_1 j^2 + c_2\sqrt{j} \ . \tag{2-8}$$

In 2003, Matveev [39] used the Howe model to calculate the damping of its experimental system and to perform the numerical analysis. The system damping coefficient used in Matveev's experimental parameters are $c_1 = 0.028$, $c_2 = 0.0001$; this damping coefficient has also used Subramanian et al. [41] in their work, giving a good comparison result. In addition, the Howe damping model has also been used by Subramanian et al. [48], Juniper [49], and Sayadi et al. [45] in the stability study and the damping coefficient is set as $c_1 = 0.1$, $c_2 = 0.06$. In the following section, these two sets of damping parameters will be used to study the stability of the Rijke type combustion system.

2.2.3. The unsteady flame heat release model

The flame located at x_f releases energy into the flow, and the heat release rate varies over time as the flow parameters change, which is the main nonlinear source in the combustion system. To calculate this unsteady heat release, researchers have proposed several empirical models, such as the Q-U model, which is a heat release and velocity model, the Q-P model which considers the heat release and pressure oscillation, and the Q-φ model[50] which considers the heat release and equivalent ratio. Fleifil [10] derived the most widely adopted linear n-τ model.

Based on Fleifil' work, the unsteady heat release rate of the premixed flame can be written as

$$Q' = n_1 u'(\mathrm{t}-\tau)\,. \tag{2-9}$$

Where n_1 and τ are the interaction index and time delay between velocity perturbation and the unsteady heat release.

The n-τ model has been verified as enabling quick prediction in linear analysis. When $-1 < n_1 u' < 1$, e.g., the velocity perturbation is not larger than the average, the range of Q' is (-1,1), but it does not consider the problem whereby once the velocity is reversed, i.e., $n_1 u' < -1$, the total heat release $\tilde{Q}$ may become negative, which is impossible in reality. Besides, Bellows measured the nonlinear mechanisms of the heat release response to imposed acoustic oscillations at a frequency of 130 Hz and concluded that the heat release rate increases with perturbation amplitude in a linear manner and saturates when u' reached 0.95 [51]. Thus, new flame models are suggested to take the saturated effect into consideration.

For nonlinear fluctuations, we need to recognize that when the flow velocity reverses, the heat release cannot be negative, and the mean value of $\tilde{Q}$ must remain equal to Q_0, therefore take Q' to have the saturation form illustrated in Eq. (2-10)

$$Q' = \begin{cases} -n_1 u_0 & \text{for} \quad u' < -u_0 \\ n_1 u' & \text{for} \quad -u_0 \le u' \le u_0 \\ n_1 u_0 & \text{for} \quad u' > u_0 \end{cases}. \tag{2-10}$$

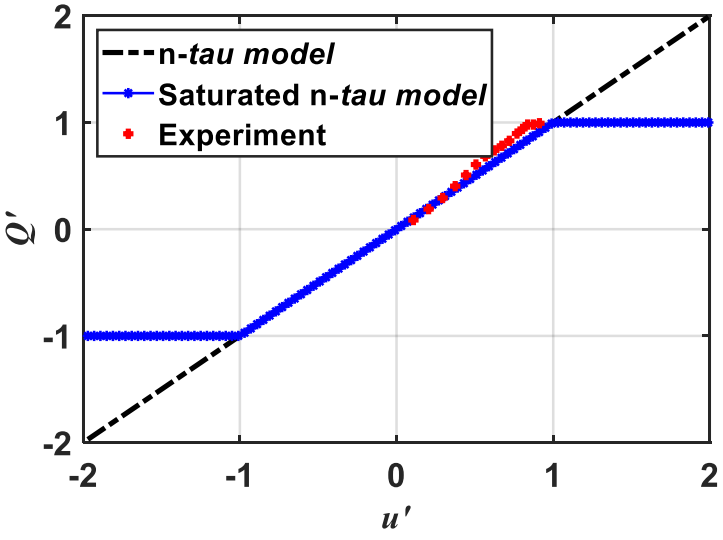

Figure 2-2 Comparison of the flame models with experiment result of Bellow.

The saturated model is a nonlinear model with upper and lower limits. It is named as 'saturated n-τ model' in this work. Figure 2-2 shows the heat release rate versus velocity perturbation of n-τ model and the saturated n-τ model with the experiment result of Bellow. It can be seen that in most of the regime (-1,1), the differences between the two models and experiment result are slight, but in the area where the absolute value of u' is larger than 1, the heat release fluctuation keeps varying with u' in n-τ model, while it is fixed at 1 for the saturated n-τ model. When u' is less than -1, e.g., the flow is reversed, the heat fluctuation is limit to -1, meaning that the total $\tilde{Q}$ is zero. With the saturated n-τ model m, that the total heat release $\tilde{Q}$ is confined between [0, $2\tilde{Q}$]. In this way, the scope of application is expanded to the area that the velocity amplitudes u' is greater than 1, and the nonlinearity is taken into consideration.

2.2.4. Boundary conditions

The pressure perturbations and velocity gradient are both zero at the ends of the tube for the Rijke typer burner with both ends acoustically opened in this study, as given in Eq. (2-11).

$$p'(x,t)\big|_{x=0}=0,\ \ p'(x,t)\big|_{x=1}=0,\ \ \frac{\partial u'(x,t)}{\partial x}\big|_{x=0}=0\text{, and }\ \frac{\partial u'(x,t)}{\partial x}\big|_{x=1}=0. \quad (2\text{-}11)$$

2.3. Galerkin approximation of the governing equations

The disturbance equations are partial differential equations in time and space. Here the Galerkin method is used to project the disturbance equations into the frequency domain and time domain with assuming a shape for the Eigenfunctions of the system as a priori. Theoretically, there will be several functions that satisfy the requirements. Here, trigonometric functions are chosen because they coincide with the acoustic modes of the tube, and the damping coefficient in Eq. (2-8), which is a function of the natural frequencies of the acoustic mode, can be easily incorporated into this method. Thus, the following applies:

$$\phi = \sum_{m=1}^{\infty} f_m(t)\psi_m(x), \text{ with } \psi_m(x) = \sqrt{2}\sin(m\pi x),\ \Omega_n = m\pi,\ m = 1,2,3\cdots\infty. \tag{2-12}$$

$$u' = \frac{\partial \phi}{\partial x} = \sum_{m=1}^{\infty} f_m(t)\cdot\sqrt{2}(m\pi)\cos(m\pi x) \tag{2-13}$$

$$p' = -\frac{\partial \phi}{\partial t} = -\sum_{m=1}^{\infty} \dot{f}_m(t)\cdot\sqrt{2}\sin(m\pi x) \tag{2-14}$$

Hence, Eq. (2-6) can be transformed to

$$\ddot{f}_n + \zeta \dot{f}_n + \Omega_n^2 f_n + \frac{(\gamma-1)\mathrm{Q}_0}{\gamma u_0 p_0}\sqrt{2}\sin\left(n\pi x_f\right)Q' = 0 \qquad n = 1,2,3\cdots\infty \tag{2-15}$$

Introducing Eq.(2-10), we will get

$$\ddot{f}_n + \zeta \dot{f}_n + \Omega_n^2 f_n + Y\sum_{m=0}^{\infty} f_m(t-\tau)\sqrt{2}(m\pi)\sin\left(m\pi x_f\right) = 0 \quad Y = n_1\frac{(\gamma-1)\bar{\mathrm{Q}}}{\gamma u_0 p_0}\sqrt{2}\sin\left(n\pi x_f\right). \tag{2-16}$$

Researchers have also considered the question of how many modes need to be retained from other perspectives. Ananthkrishnan et al. investigated the energy transfer between acoustic modes[52], and Wang et al.[53] applied the pseudospectral-method-based model reduction approach proposed by Frankel et al.[54] to solve this problem. The time evolutions of the systems with different numbers of acoustic modes are compared in Figure 2-3.

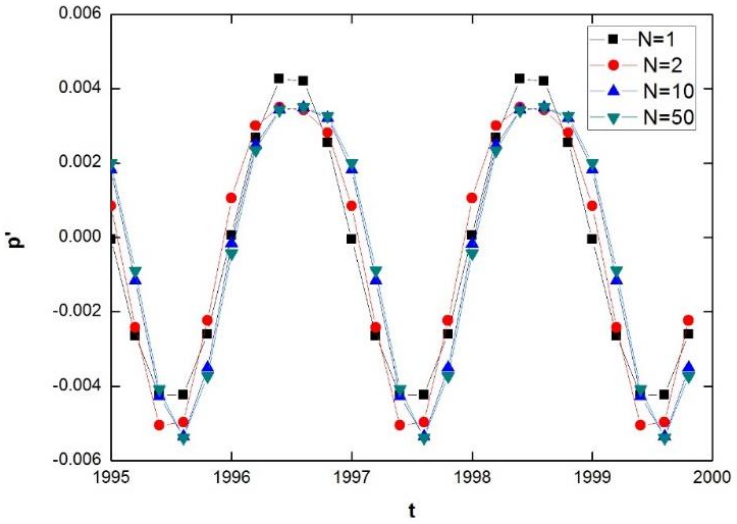

Figure 2-3 Comparison of time evolution of the system with different acoustic Galerkin mode

numbers. The parameter values of the system are: x_f=0.25, q_0=25000, n_1=0.25, u_0=0.14, c_1=0.048,c_2=0.015, γ=1.389， ρ_0=1.236, a_0=357, Rg=287, τ=0.5.

It can be seen that the amplitude of the limit cycle shows minimal variation when the number of Galerkin modes increases from 10 to 50, which means a modal convergence in capture the nonlinear behavior accurately. Thus, 10 Galerkin modes are used in this work.

2.4. Results and discussions

Concepts from nonlinear dynamics and complex systems theory could reveal the nature of coupling among flow, combustion, and acoustic fields and identify the most sensitive points. Some of the nonlinear methods applied in this research are listed as follows.

Time series of the pressure oscillations and the total heat release rate of flame at given conditions can reveal the state of the combustion system directly. Once the time series data obtained from simulation, stability analysis could be performed consequently.

Eigenvalues can be used to study the stability of a system's solution. For a given system, if all the roots have a negative real part as shown in Figure 2-4(a), the solution will then be stable, whereas if there are one or more roots with a positive real part, as shown in Fig. Figure 2-4 (b), the system will be unstable. If the eigenvalues move through the imaginary axis as one or more parameters are changed, bifurcation occurs. Generally, a fold bifurcation occurs when the root is real (namely, equal to zero), and a Hopf bifurcation occurs when a pair of complex conjugate roots cross the imaginary axis. The value of the parameter at which a bifurcation occurs is called the bifurcation point.

Bifurcation diagrams show the changes in the nature of solutions to the governing equations as control parameter changes. From a bifurcation diagram, the types of stable oscillations could be identified as period-1, period-n, quasi-periodic, frequency lock, and chaotic oscillations. In bistable regions, hence mode switching and hysteresis are possible.

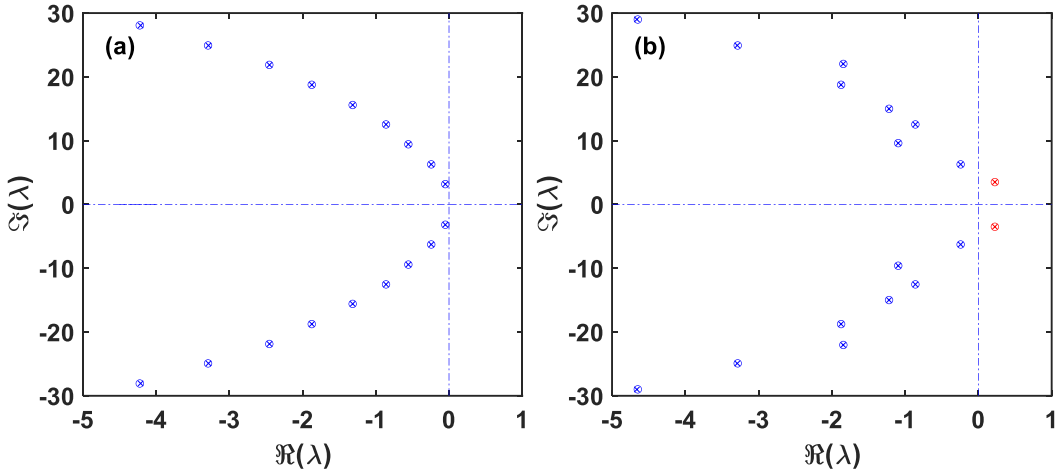

Figure 2-4 Comparison of the eigenvalues of stable and unstable systems. (a) Eigenvalues of a stable system, (b) eigenvalues of an unstable system. The horizontal and vertical axes are the real and imaginary parts, respectively, of the system eigenvalues λ.

Phase space reconstruction and Poincaré sections can represent the different types of oscillation distinctly. In addition, they can identify if an attractor is stable or not. Phase space reconstruction and Poincaré sections are more valuable than simply examining time series or power spectra because the well-defined topological structure of attractors can be used to obtain quantitative information about the system's nonlinear behavior.

2.4.1. The stability of system under given parameters

Apparently, Eq. (2-15) has a zero solution under any parameter values, which is the equilibrium state of the system. The stability of this zero solution can be determined by calculating its characteristic equations and eigenvalues. Because of the time delay in the flame model, Eq. (2-15) is a delay differential equation (DDE), and its characteristic equations usually exhibit an infinite number of eigenvalues.

In Eq. (2-16), let Y=0.06, c_1=0.048, c_2=0.015, and τ=0.2. Two cases with different initial conditions are compared. The initial conditions of case A are $f_1 = 1,\ f_i = 0\ \forall i = 2,3,4 \dots N$ and $\dot{f}_i = 0, \forall i = 1,2,3 \dots N$. The initial conditions of case B are $f_1 = 0.001,\ f_i = 0\ \forall i = 2,3,4 \dots N$ and $\dot{f}_i = 0, \forall i = 1,2,3 \dots N$. There is only one difference between these two cases, which is the different amplitude of the initial velocity disturbance. It can be seen that under the two initial conditions，the system finally evolves into steady state. The eigenvalues are then computed with DDE-

BIFTOOL[55],[56], which is a MATLAB package for numerical bifurcation analysis of steady-state and periodic solutions of systems of DDEs written by Engelborghs. The results are shown in Figure 2-5. All the eigenvalues are in the left half the complex plane. Thus we can conclude that this is a stable case. Thus, for any pertubations, the system will finally become steady.

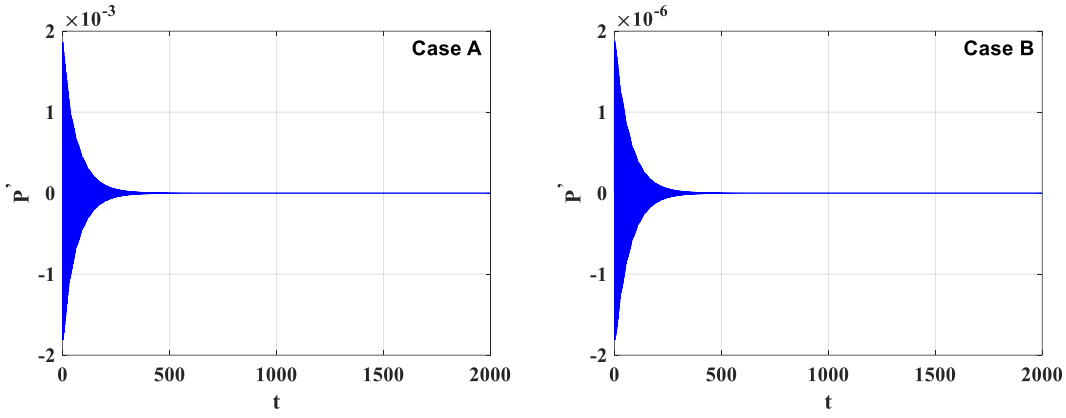

(a) Time evlotion of Case A (b) Time evlotion of Case B

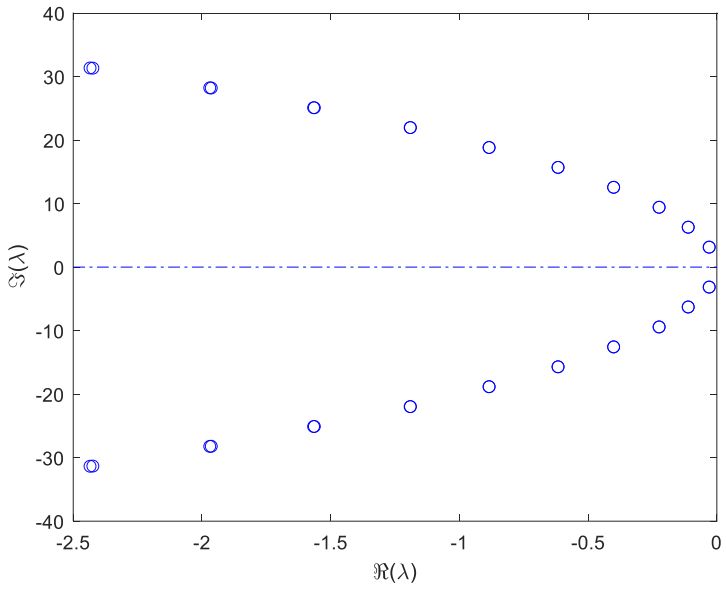

(c) The eigenvalues of the system

Figure 2-5 The eigenvalues of the system with parameter values of the system as c_1=0.048, c_2=0.015, τ=0.2, Y=0.06.

Next, let Y=0.11, c_1=0.048, c_2=0.015, and τ=0.2. Also, two cases C and D, with different initial conditions, are compared, which are the same setting A and B, respectively. The results are given in Figure 2-6 (a) and (b). In case C, the system amplitude decays at

first but finally maintains in a tiny amplitude about 0.8×10^{-3}. In case D, since the initial perturbation is very small, the system does not decay at first. However, the oscillation gradually increases with time with a very small variety. These results mean that the final state of the system does not only depend on the parameters but also influent by the initial conditions. After 2000 steps, the increase in amplitudes is just 0.1×10^{-6}. In Figure 2-6 (c). It can be seen that there are a pare of Conjugate complex roots with a zero real part, showing that this is the bifurcation point of the system.

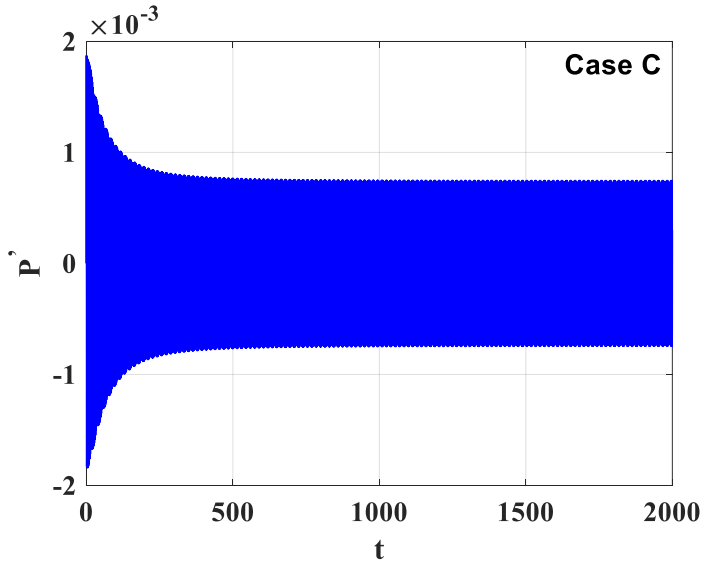

(a) Time evlotion of Case C

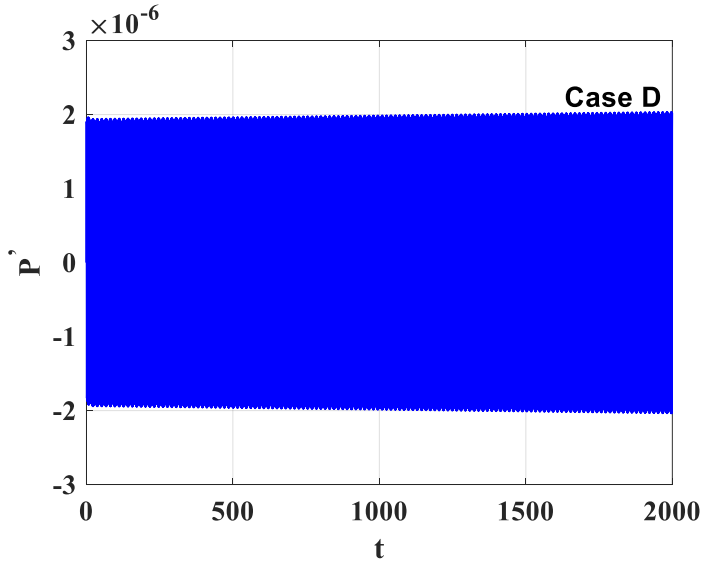

(b) Time evlotion of Case D

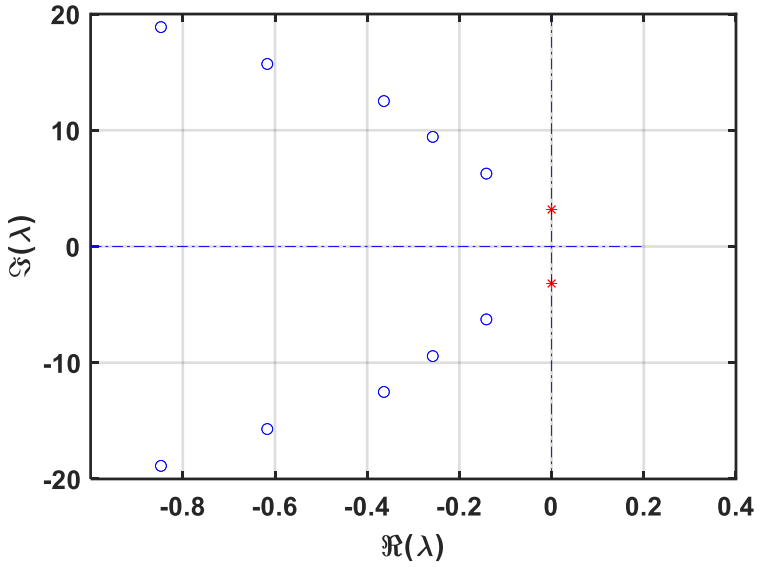

(c) The eigenvalues of the system

Figure 2-6 The eigenvalues of the system with parameter values of the system as c_1=0.048, c_2=0.015, τ=0.2, Y=0.11.

Figure 2-7 show the system's eigenvalues with Y=0.2, c_1=0.048, c_2=0.015, and τ=0.2. Once again, two cases E and F, with different initial conditions, are compared. The initial conditions of case E are $f_1 = 1,\ f_i = 0\ \ \forall i = 2,3,4 \dots N$ and $\dot{f}_i = 0, \forall i = 1,2,3 \dots N$. The initial conditions of case F are $f_1 = 0.001,\ f_i = 0\ \ \forall i = 2,3,4 \dots N$ and $\dot{f}_i = 0, \forall i = 1,2,3 \dots N$. The time evlotion of the pressure amplitudes of both these two cases shown in Figure 2-7 (a) and (b) increase rapidly and finally maintain in the same amplitude. In Figure 2-7 (c), there are two pares of Conjugate complex roots with positive real parts, showing that zero solution is the unstable solution of the system under this case. It means that for any perturbations, the system will finally evolve into the limit cycle oscillation state with the same amplitude. These results can be proved by the bifurcation plot shown in Figure 2-8 in the following part.

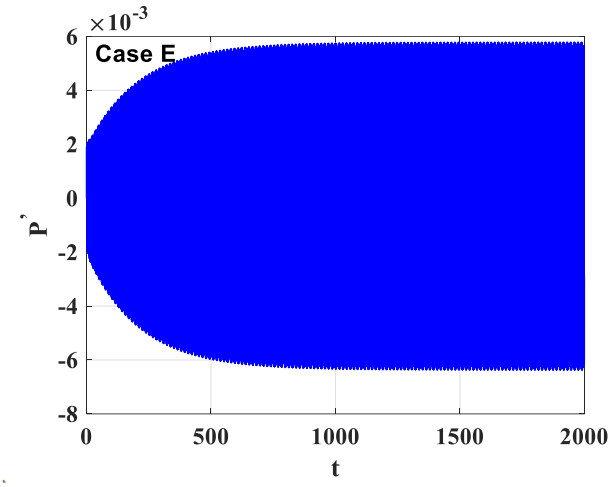

(a) Time evlotion of Case E

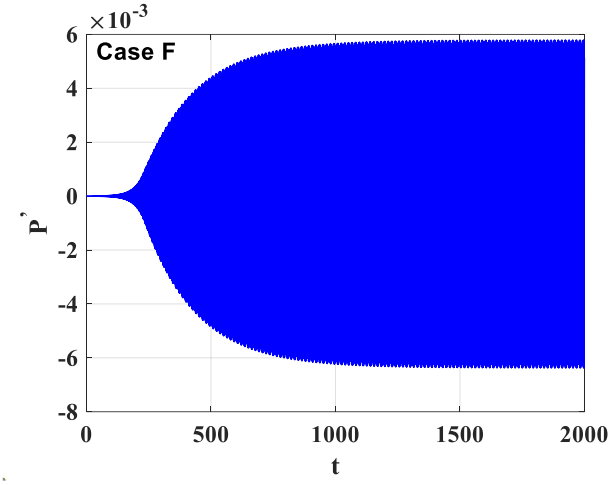

(b) Time evlotion of Case F

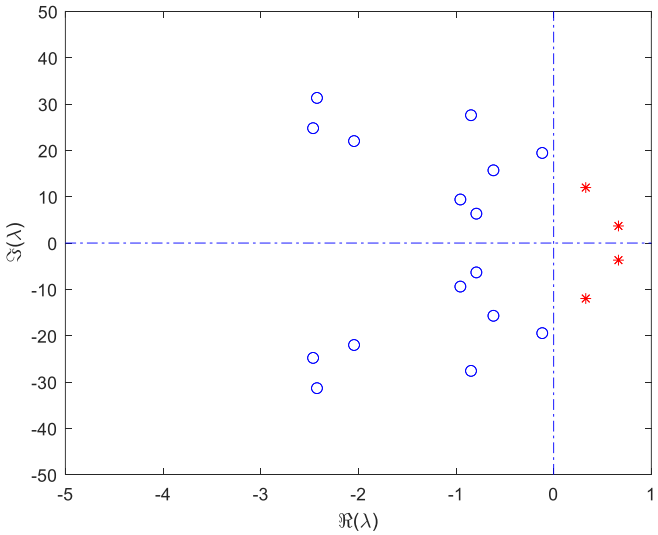

(c) The eigenvalues of the system

Figure 2-7 The eigenvalues of the system with parameter values of the system as c_1=0.048, c_2=0.015, τ=0.2, Y=0.2.

2.4.2. Effect of the average heat release intensity

The bifurcation analysis of the effect of the average heat release intensity on the system stability is studied here. Figure 2-8 presents the bifurcation diagram of self-excited oscillation with Y as the control parameter, where f_1 denotes the maximal value of the first mode in the tube, and it connects with the maximal velocity mode. Y is related to average heat release, and a large Y means the average heat release is high. In Figure 2-8, the parameters are settled as following: x_f=0.3, c_1=0.048, c_2=0.015, τ=0.2, and the initial condition is set as $f_1 = 0.01,\ f_i = 0\ \ \forall i \neq 1$, and $\dot{f}_i = 0\ \ \forall i = 1, \cdots N$.

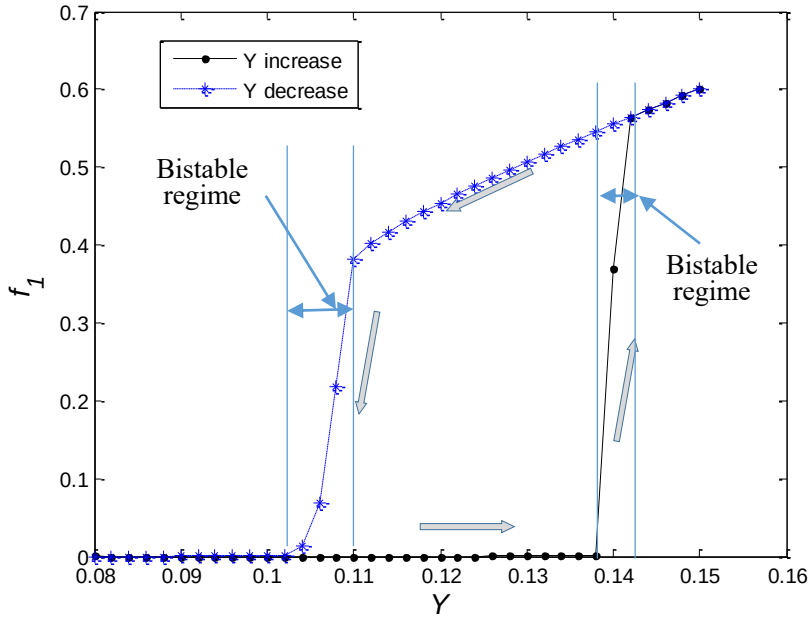

Figure 2-8 Subcritical Hopf bifurcations in the Rijke burner. The solid line indicates the power increase case, and the dashed line indicates the power decrease case.

First, the average power of the burner is increased by increasing Y from 0.8 to 0.15, then we decrease Y from 0.15 to 0.8, as the gray arrows show in Figure 2-8. Every time when Y is changed, the amplitude of f_1 in the last step is set as the initial condition of the new step. Apparently, this system has two subcritical Hopf bifurcation regimes. When Y<0.102, the system has one stable solution with a zero-fluctuation magnitude. This regime is called the subthreshold regime. When 0.102<Y<0.11, and

0.138<Y<0.142, the system is bistable, it has two stable solutions, one is a limit cycle with finite amplitude and the other is zero, whether the system will be excited is depending on the amplitude of the perturbation. When 0.11<Y<0.142, the system has one stable result, e.g., the limit cycle solution, indicating that even a tiny perturbation may lead the system to be excited into an oscillating state. When Y>0.142, the system has only one stable solution. The subcritical Hopf bifurcation here is caused by the time lag between velocity fluctuation and combustion heat release and called the hysteresis effect, which existed in many nonlinear thermoacoustic systems.

2.4.3. Effect of flame location

Flame location is a crucial factor that affects the dynamic behavior of the Rijke burner too. The effect of flame location x_f is investigated and presented in Figure 2-9. In Figure 2-9, the parameters are settled as following: c_1=0.048, c_2=0.015, τ=0.2, the initial condition is set as $f_1 = 0.01,\ f_i = 0\ \forall i \neq 1$, and $\dot{f_i} = 0\ \forall i = 1, \cdots N$. Here the dynamics of system is calculated under three level of heat release intensity: Y=0.08 Y=0.12, and Y=0.15. It can be seen that for a given Y, there is a critical value that the system will be stable when x_f is small than it, and will be oscillating when x_f is bigger than it. This phenomenon is called supercritical bifurcation. With the increase of Y, the excited regime is enlarged while the oscillation amplitude is increased too. When x_f <0.12 and x_f>0.38, the system is stable, and it is not affected by the heat release intensity. However, when 0.12< x_f <0.38, the system is in an oscillating regime, whether the system will evolve into an oscillating state, and the oscillating amplitude is related to the heat intensity.

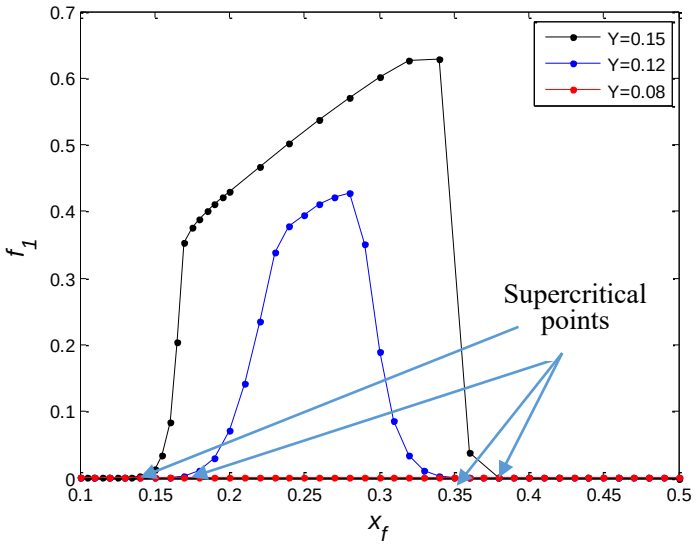

Figure 2-9 Supercrticial bifurcations for variation of flame location (x_f)

2.4.4. Effect of time delay

In some cases, it was found that the time delay does not have an important influence on the system behavior [22]. However, the study in this work has shown that the time delay between unsteady heat release and velocity perturbation can affect the stability prediction greatly. The stability of the time delay is numerically studies, and the parameters are chosen to be x_f=0.25, q_0=25000, n_1=0.25, u_0=0.14, c_1=0.048, c_2=0.015, γ=1.389, ρ_0=1.236, a_0=357, Rg=287. The initial status is set as $f_1 = 0.01$, $f_i = 0 \ \forall i \neq 1$, and $\dot{f}_i = 0 \ \forall i = 1, \cdots N$. Figure 2-10 shows the time evolution of system response when time delay continuously increasing. In Figure 2-10 (a), when τ is very small, the initial disturbance decays to a stable status rapidly. With the increase of τ, the rate of decay declines, just as Figure 2-10 (b) shows. The system becomes unstable until τ = 0.19 in Figure 2-10 (c), Then the amplitude of oscillation increases with τ. When τ equals 0.5, as in Figure 2-10 (d), the amplitude reaches a maximum value. Then the amplitude begins to decrease with τ as in Figure 2-10 (e), until in Figure 2-10 (f) τ = 0.82, the system comes into a stable regain again. When increasing the time delay to the next critical point, it will become unstable again. This phenomenon is called stability switching, e.g., the system's stability switches in stability and instability while keeping varying the time delay.

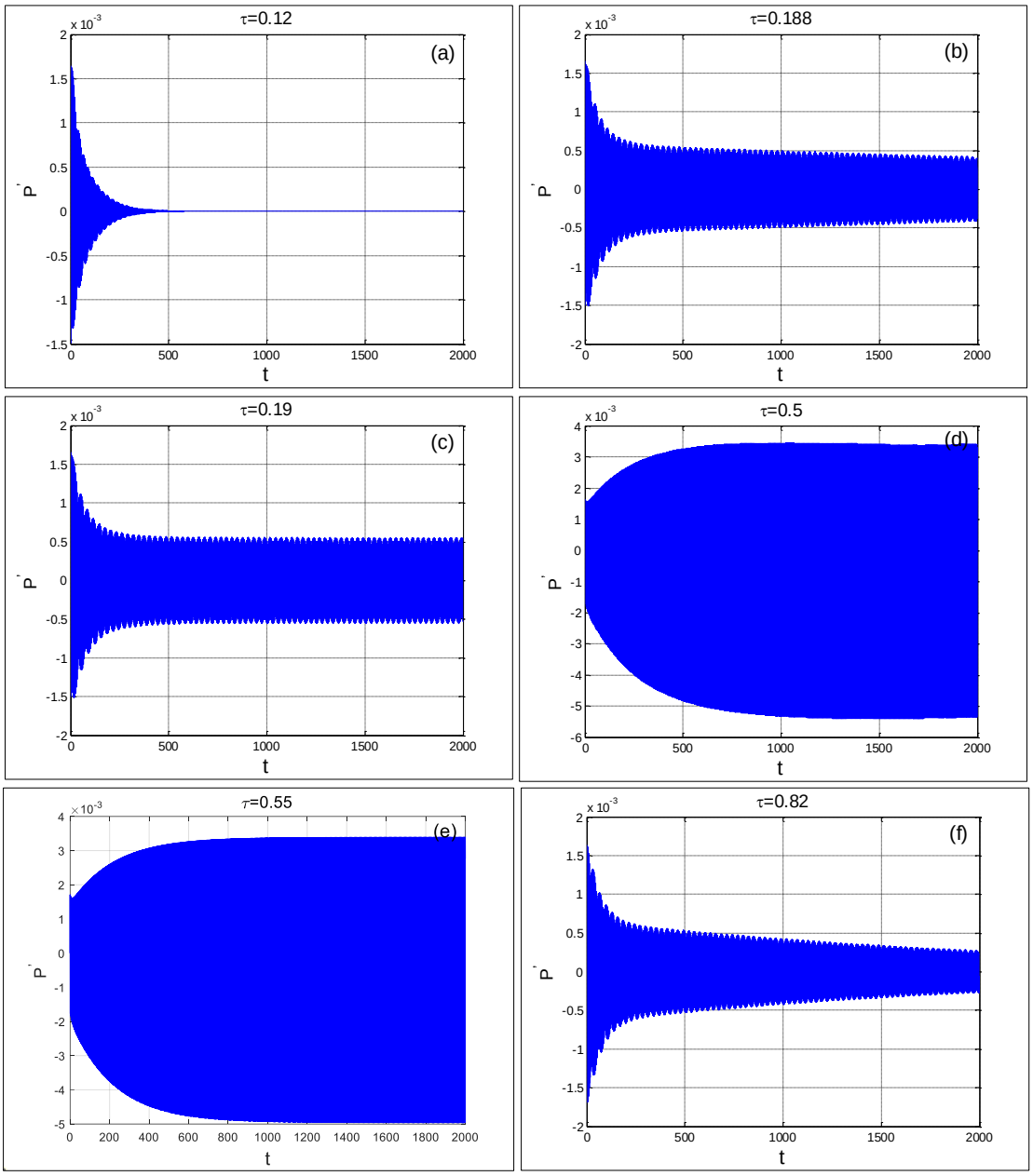

Figure 2-10 Time evolution of the Rijke type burner with different time delays

Li et al. have found a similar phenomenon in their research, but they failed to get the limit cycle because the flame model they adopted is a linear model [23]. In Figure 2-11, The effect of varying the time delay on the amplitude of the acoustic modes is analyzed. Since the amplitudes of higher-order modes of pressure perturbation are really small, here, only the first three modes are presented. It can be seen that the amplitudes of the first three modes are varying with time delay. There are several stability regions and instability regions in Figure 2-11. This phenomenon is called stability switching behavior, e.g., the stability of the system is switching between stability and instability.

We have to be aware that this stability switching is not periodical because when $\tau > 5$, the system keeps stable and does not vary anymore.

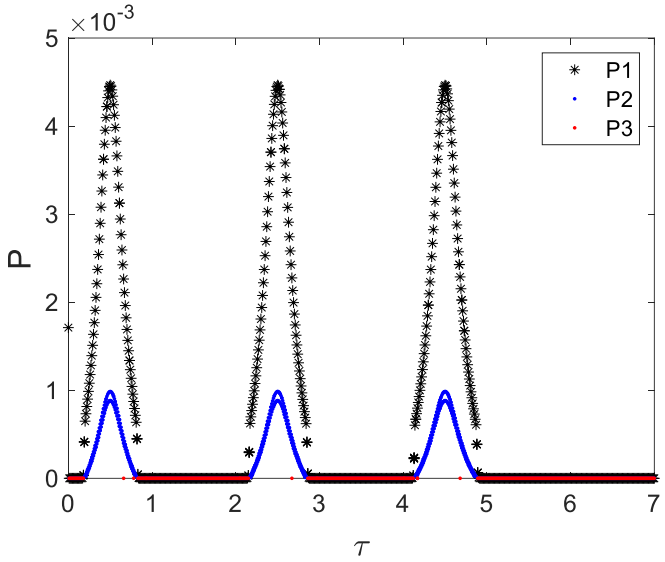

Figure 2-11 Bifurcation plot for variation of time delay (τ).

The frequency content of the case shown in Figure 2-10 (d) is calculated by the FFT method and shown in Figure 2-12. It can be seen that the first and second harmonics are excited, which agrees with Figure 2-11 at τ =0.5.

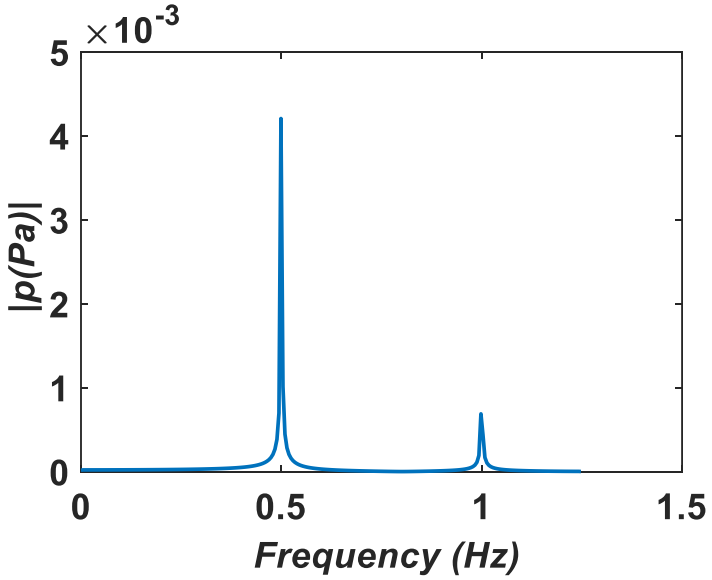

Figure 2-12 Frequency plot of the calculated pressure with the parameter set in Figure 2-10 (d)

2.4.5. The Phase diagram and Poincaré map

The phase trajectory of a state variable $\boldsymbol{x}$ and its derivative ($\dot{\boldsymbol{x}}$, $\ddot{\boldsymbol{x}}$...) in the phase plane

or phase space during the transition process of the system is called the phase diagram. It can be used to study the dynamic process of the system intuitively. For example, it can judge whether a system is stable by observing whether the phase trajectory converges.

Poincaré map (also called 'first recurrence map') is named after Henri Poincaré. It is an effective method in the analysis of nonlinear dynamical systems. The main feature of Poincaré map is that it can transform a continuous system into a corresponding discrete system for analysis and reduce system dimension from n dimensions to a certain low-dimensional subspace, which effectively simplifies the analysis of the dynamic characteristics of high-dimensional systems.

Poincaré used a cross-section to cross the trajectory of a continuous motion, and the form of the motion could be judged according to the trajectory passing through the section. Suppose the point $X(n)$ is the point where the trajectory crosses the cross-section for the n^{th} time, then the point $X(n+1)$ can be regarded as a mapping of $X(n)$, $X(n+1)=f(X(n))$ $n=0,1,2\ldots$. If there is only one intersection point between the trajectory and the cross-section, the system is a period solution. If there are two or four fixed points on the Poincaré map, then the system is a period-2 or a period-4 solution. If the Poincaré cross-section is a closed circle, the corresponding system is a quasi-periodic solution; and if the Poincaré cross-section diagram has an obvious hierarchical structure, in the case of a fractal structure, the system is a chaotic solution.

The phase space trajectory and Poincaré map of time evolution in Figure 2-10 (d) are drawn in Figure 2-13. The phase plot in Figure 2-13 (a) shows a limit cycle with period-1, and in Poincaré map, there is one fixed point.

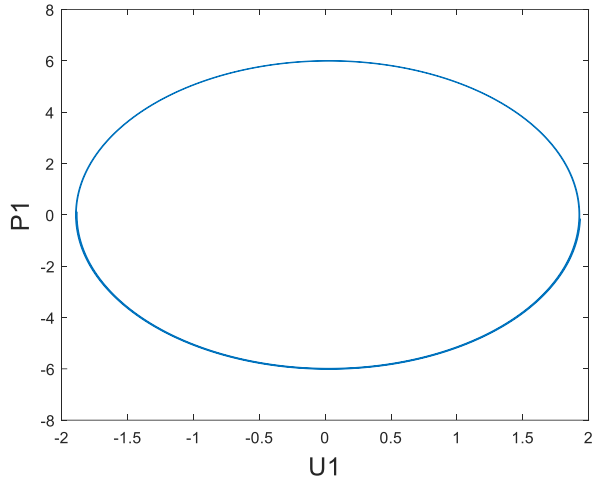

(a) phase diagram

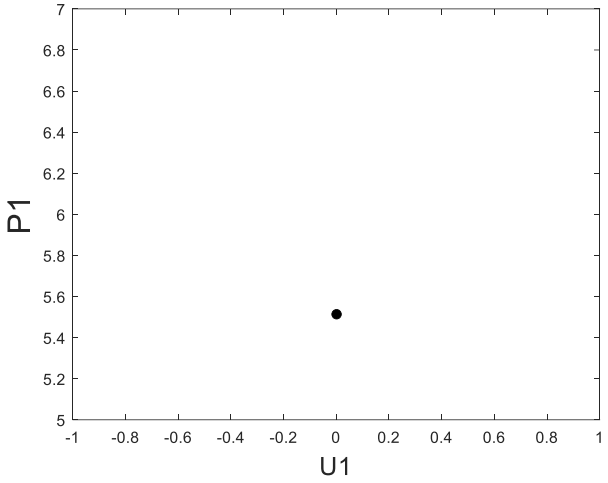

(b) Poincaré map

Figure 2-13 Phase diagram and Poincaré map with the parameter set in Figure 2-10 (d).

2.4.6. The growth rate of the oscillation

The acoustic disturbances growth rate is a very important parameter for the combustion systems. The previous linear model can predict the frequency but can't calculate the oscillating amplitudes and growth rate. The saturated n-τ model overcomes this defect. Figure 2-14 and Figure 2-15 show the growth rate of the pressure oscillation in Figure 2-10 (a) and (d), which represent a perturbation decay case and a self-excited oscillation case, respectively. The local maximum and minimum values of the pressure are identified, Exponential functions are constructed to fit best the series of these peak values. They are written as:

$$p_L = \pm Ae^{\alpha t} \tag{2-17}$$

where p_L is the series of local maximum and minimum pressure, A, α, are parameters to be solved by iteration. The results are as following: the calculated exponential growth rate for the case in Figure 2-10 (a) is -0.012, and 0.035 for the case in Figure 2-10 (d).

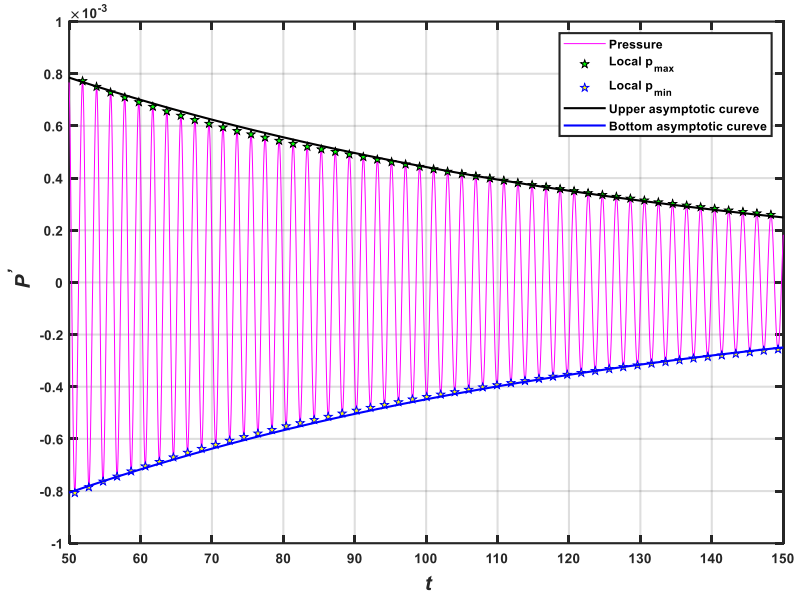

Figure 2-14 Time evolution of the pressrure oacillation in the decay case and the growth rate fitting curve of Figure 2-10 (a)

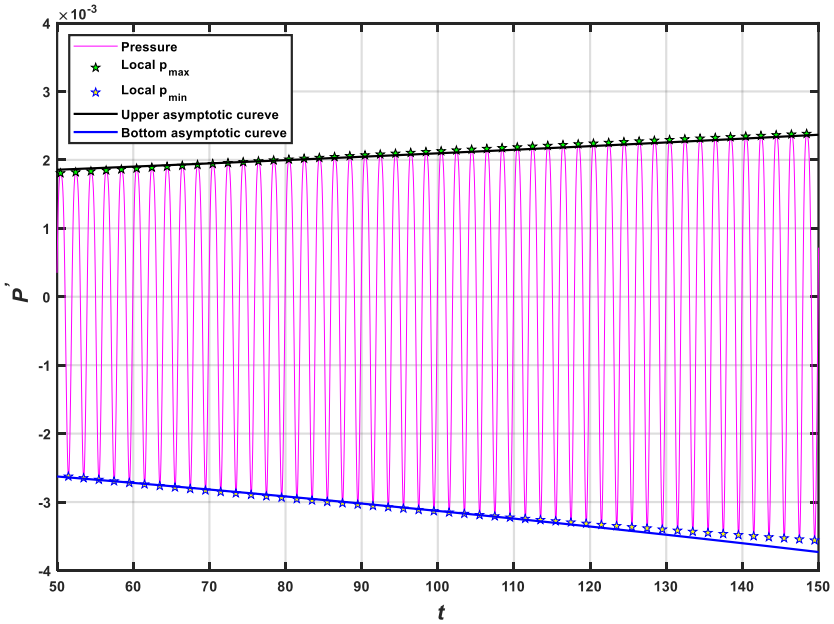

Figure 2-15 Time evolution of the pressrure oacillation in the inscrease stage and the growth rate fitting curve of Figure 2-10 (d)

2.5. Conclusions

The nonlinear analysis of the combustion instability is conducted in this work. With the nonlinear flame model proposed in this work, the typical nonlinear dynamic behaviors, including the self-oscillations, supercritical bifurcation, subcritical bifurcation, limit cycle oscillation, and the stability switches in the combustion system, are captured. Th following conclusion can be obtained.

1) Eigenvalues can help to determine the stability of a given system.

2) The system shows subcritical bifurcation characters when varying the flame location, and there are bistable regions in the location-amplitude plot.

3) The unstable area of the system enlarges, and the oscillating amplitude increases with the increase of heat intensity under a given heat source location and time delay since more heat energy is converted into sound energy.

4) The system stability switches between stability and instability as the time delay increases under given heat source location and heat source intensity cases, which is called stability switching and is a typical nonlinear phenomenon in a delay-dependent system.

5) The phase diagram and Poincaré map are helpful tools in the study of the dynamic process of the system intuitively.

In conclusion, the nonlinear methods, including the eigenvalues, bifurcations diagrams, the phase diagram and Poincaré map, and the exponential growth rate, are used in this section. These nonlinear analytical methods help to understand the nature of combustion instability.

3. CFD Simulation of combustion flow

3.1. The introduction of CFD method

CFD simulation is the branch of fluid mechanics that use computers and numerical method of discretization to solve and analyze the fluid dynamic problems. It provides a virtual laboratory to perform experiments. Almost all the CFD problems are based on the Navier-Stokes equations. By solving the N-S equations, people can get the flow parameters such as pressure, velocity, temperature, energy. However, unfortunately, N-S equations are a set of partial differential equations, usually cannot be solved by analytical methods to get exact solutions. The numerical method is to approximate the continuous accurate solutions through the approximate solutions on the discrete nodes. The general procedure of CFD research consists of the following steps:

1) Define the modeling goals. Researchers need to simplify the complex problem by keeping the main factors while ignored the unimportant ones.

2) Design the model geometry and discretize it by generating an appropriated mesh. The number of nodes affects the accuracy of the calculation results and the size of the calculation consumption. Generally speaking, as the number of grids increases, the calculation accuracy will be improved, but the calculation time and memory requirement will also increase. Therefore, these two factors should be considered when determining the number of grids.

3) Set up the physical modes such as the governing equations, boundary conditions, initial conditions, material properties, and other parameters. All the parameters appearing in the governing equations must be defined appropriately here.

4) Program the numerical calculation (this can be skipped if using existing software). In this step, the governing equations are discretized on the temporal and spatial domain. There are three primary discretion methods, namely, the

finite volume method (FVM), finite element method (FEM), and finite difference method (FDM). Among them, the FDM and FVM are more popular.

5) Computer and monitor the solution. This step usually takes several hours or even several weeks, depending on the complexity of the problem to be solved, the node numbers, and the computing resources.

6) Post-processing of calculation results. The CFD program or software writes the calculation results into specific data files, which usually include the coordinates and relationships of the mesh nodes and the flow parameters on each node. Researchers need to use specific tools to visualize the grid structure and flow field parameters. Besides, the results need to be verified, compared with experiments or previous cases, and evaluated.

CFD can be applied to a wide range of research, including aerodynamics and aerospace analysis, weather simulation, natural science and environmental engineering, industrial systems such as turbomachinery, biological engineering, heat transfer, and engine and combustion analysis. The commonly used CFD methods include finite element method, finite difference method, finite volume method, boundary element method, spectral element method, and Lattice Boltzmann method, etc. It can solve problems of laminar flow, turbulence flow, flow stability, nonlinear flow, etc. With the development of computational technology, CFD simulations can simulate the reacting flow, radiation, acoustics, solidification, and melting at present, increasingly helping to describe the mechanisms of complicated fluid dynamics and to provide guidance for experimental research. Compared with the experimental method, the CFD method can save resources and time significantly. With these advantages, the CFD method has become a powerful tool for studying fluid problems, and many large commercial CFD softwares are developed and have been wildly used. In the simulation of a combustion flow, several issues, including but not limited to the fluid dynamics, the turbulence, the chemical reaction, the heat transfer, the radiation, and the acoustics, should be taken into

consideration. Thanks to the advancements of computers, the simulation of reacting flow has developed fastly in recent years. Many 2-D or 3-D combustion flow are simulated to determine all the parameters in detail[57]-[59] for further analysis, such as pollution control, efficiency enhancement, and mass transport processes[60]-[61].

The present study concentrates on the CFD simulation of a 2-D Rijke burner to understand the dynamics of self-excited thermoacoustic instability. A finite-volume-based approach is used to simulate reacting. The onset of growth of the pressure, velocity, and reaction heat are captured. The oscillation frequency and mode are calculated and compared with the theoretical prediction, and they show good agreement. Finally, the unsteady flow fields at different times show that flame-induced vortices occur inside the combustor, and the temperature distributions show that the velocity perturbation in the tube changes the distance between the flame and honeycomb in turn, forming a forward feedback loop in the tube. The results of this work show that there are vortices in the Rijke-type burner when thermoacoustic instability occurs.

3.2. CFD simulation of reacting flow

3.2.1. Physical model and grid generation

The Rijke burner used in this study consists of a 1572 mm-long steel tube with an inner diameter of 73.7 mm, as shown in Figure 3-1. A premixed methane-air mixture is fed into the inlet end of the tube, and a honeycomb flame stabilizer with a thickness of 25.4 mm is positioned in the middle of the tube. A flat flame is anchored at the top of the honeycomb flame stabilizer and release unsteady heat into the flow, inducing pressure oscillation in the tube. The length-to-diameter ratio is more than 20, which can ensure the acoustics mode can be simplified to 1D.

The flow field in this burner is a 3D problem, while both the structure and boundary conditions are axisymmetric to the centerline of the tube. Thus, a 2-D axisymmetric flow field is used to approximate this 3D flow field to simplify the computational model, as shown in Figure 3-2. The 3D honeycomb flame stabilizer is approximated by 2D

channels while keeping the area restriction constant.

In Figure 3-1 the Rijke burner is installed vertically while the computational field in Figure 3-2 is a horizontal domain, that is because that the axisymmetric axis should be set on the *x*-axis in the software.

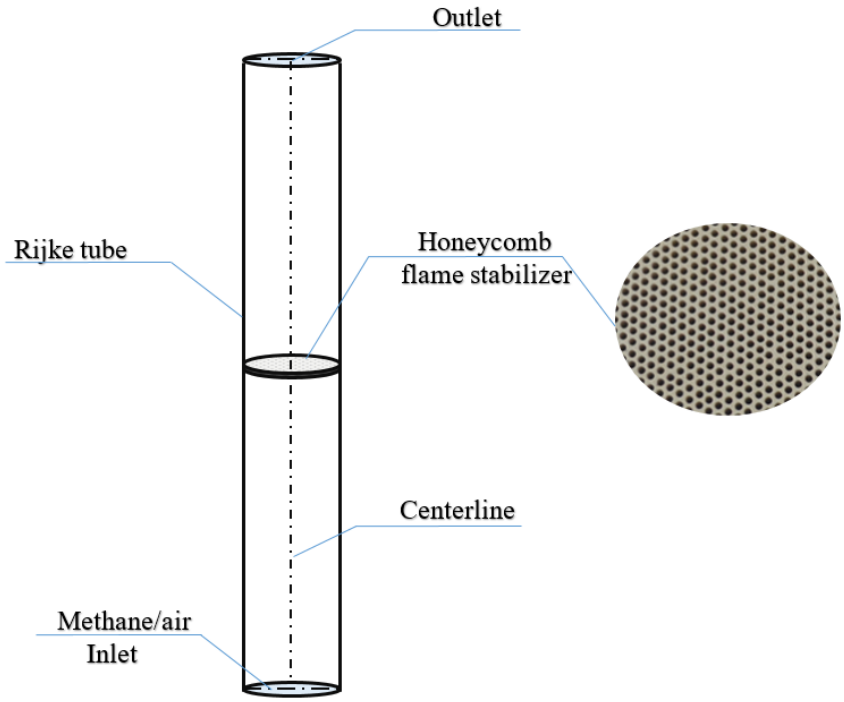

Figure 3-1. Schematic of the Rijke burner and the honeycomb flame stabilizer (not to scale)

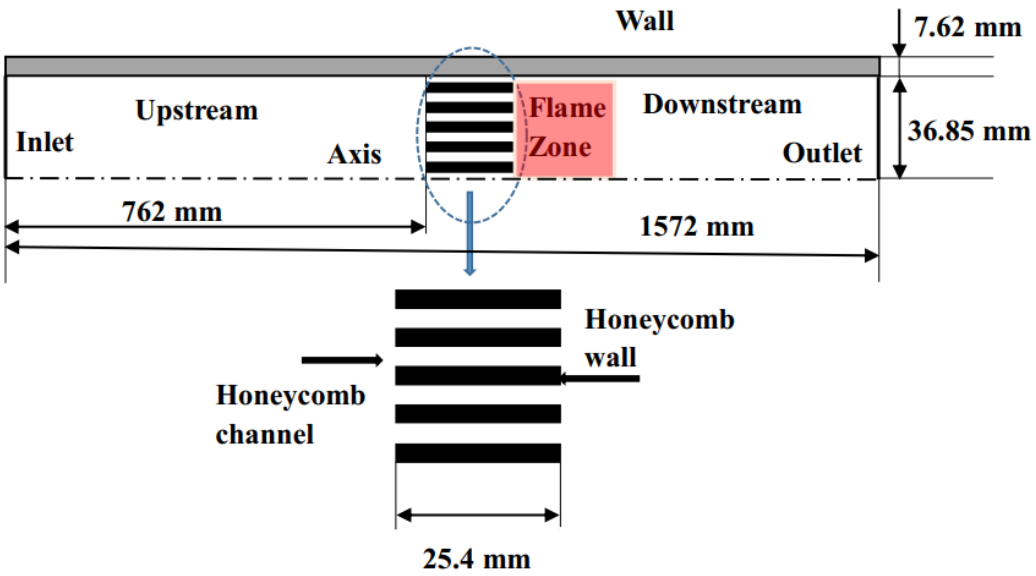

Figure 3-2. Configuration of the axisymmetric Rijke burner model (not to scale).

3.2.2. Mesh generation

There are two points that need to be taken into consideration for spatial discretize :

1) The flow field has a high length-to-diameter ratio, requiring the size of the discrete mesh must be small enough to set enough points in the radial direction. The aspect ratio, which refers to the relationship between the width and height of a grid cell. If the aspect ratio is too high, the mesh may become flat or deformed, which affects the accuracy of the results. Then the mesh size in the axial direction cannot be too large. As a result, the number of mesh nodes must be huge.

2) The reaction occurs on very thin surfaces. Thus, the mesh should be highly fine in the reaction zone, while in the upstream and downstream areas that are far away from the reaction zone, the mesh can be relatively coarse.

Thus, a hybrid grid scheme is applied. Structured mesh with different sizes is generated in the upstream area, the flame stabilizer area, and the downstream area, while the unstructured mesh is generated in the area of the reaction zone and near the inlet and outlet face of the flame stabilizer zone. The mesh of the whole computational domain is in Figure 3-3(a), and the local mesh near the flame stabilizer and reaction zone is shown in Figure 3-3(a) to make it clear. It can be seen that the quantity of nodes near the flame stabilizer is much more than that in the upstream and downstream areas.

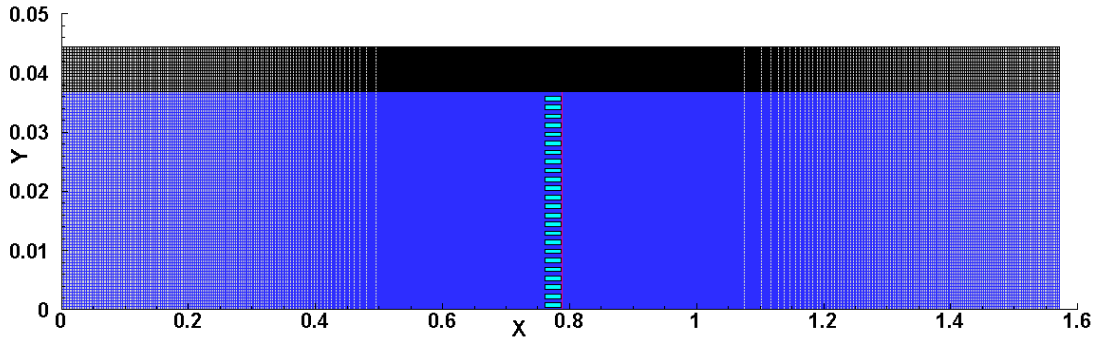

(a) Global view of the mesh structure

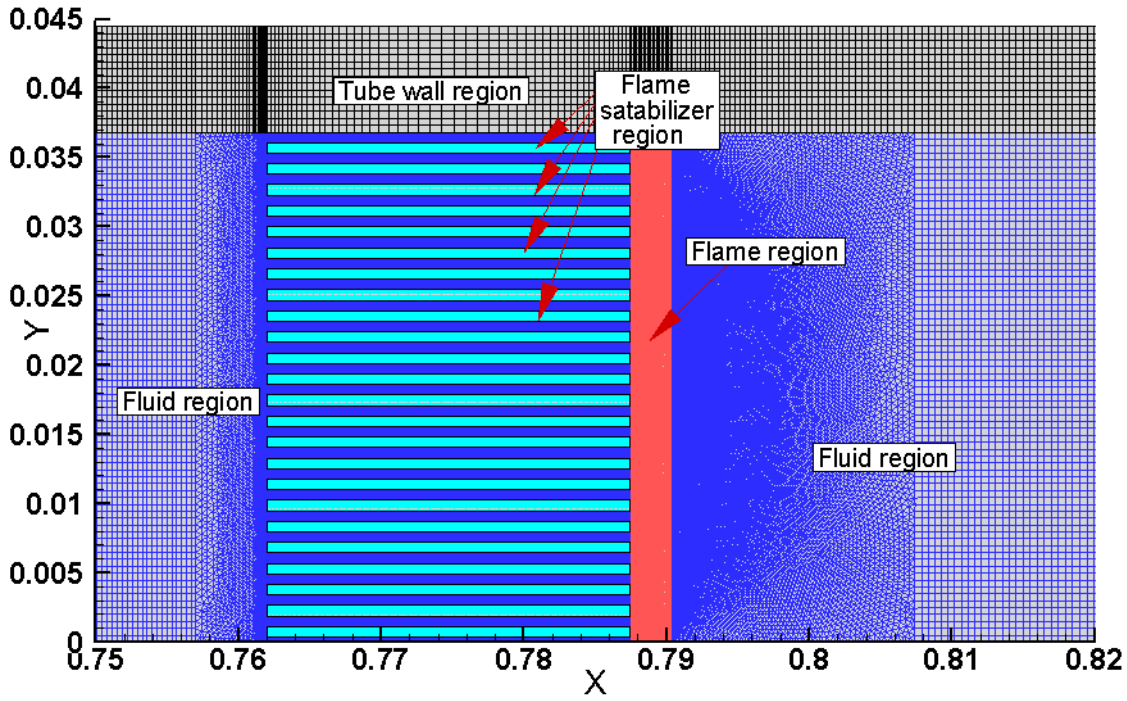

(b) Close view of the flame area

Figure 3-3. The hybrid mesh near the flame stabilizer region and reaction region (the black, red, dark blue, and light blue colors represent the mesh of tube wall region, flame region, fluid region, and flame stabilizer region, respectively.).

3.2.3. Flow modeling and boundary model

The model of the Rijke burner is generated, and boundary conditions are set, including the mass flow rate inlet, pressure outlet, coupled wall between the honeycomb and flow, coupled wall between the inside tube wall and flow, outer tube walls, and axisymmetric centerline. The input parameters used in setting up the Rijke burner mode are as follows: The incoming flow is set to 1.27×10^{-4} kg/s with a fuel/air equivalence ratio of 0.75. The equivalence ratio is defined as the value of the actual fuel/air mass ratio relative to the stoichiometric fuel/air ratio. If it is less than 1, the combustion is lean with excess air. The convective heat transfer coefficient for the outside tube wall is estimated to be 20 $W/(m^2\cdot K)$, and the reference condition is set as normal temperature and pressure. The boundary conditions are summarized in Tables 3-1.

Table 3-1. Operational conditions for the Rijke burner simulation

Boundary	Boundary condition	Parameter setting
Inlet	Uniform and steady velocity Acoustically closed	1.27×10^{-4} kg/s $u' = 0$ m/s
	Fuel-air mass fractions	CH_4: 0.04197 O_2: 0.22323 ($\Phi = 0.75$)
	Temperature of the mixture	293K
Outlet	Atmospheric pressure Acoustically open	0 Pa (gauge pressure)
	Species mass fractions	O_2: 0.23292
Inside tube wall	Coupled between the fluid flow and the adjoining solid wall	
Outside tube wall	Convection coefficient	20 W/(m^2·K)
Flame stabilizer wall	Coupled between the fluid flow and the adjoining solid wall	
Centerline	Axisymmetric boundary	

The governing equations of this model include conservation equations of mass, kinetics, species, and energy, combined with radiation equations. The conservation equations are expressed by

1) Mass conservation

$$\frac{\partial \rho}{\partial t} + \nabla \cdot (\rho \vec{u}) = 0, \tag{3-1}$$

where ρ, $\vec{u}$, And t are the density, velocity, and time, respectively.

2) Species transport equation

$$\frac{\partial (\rho Y_i)}{\partial t} + \nabla \cdot (\rho \vec{u} Y_i) = -\nabla \cdot (\vec{J}_i) + \dot{w}_i + S_i, \tag{3-2}$$

where Y_i is the mass fraction of species *i*, $\vec{J}_i$ is the diffusion flux induced by the temperature and concentration gradients of species *i*, $\dot{w}_i$ is the net production rate of species *i* by combustion reaction, and S_i is the source of species *i*.

3) Momentum conservation

$$\frac{\partial(\rho\vec{u})}{\partial t} + \nabla \cdot (\rho\vec{u}\vec{u}) = -\nabla \cdot (p) + div(\tau) + \rho\vec{g} + \vec{F}, \quad (3\text{-}3)$$

where τ is the stress tensor, $\rho\vec{g}$ is the gravitation term, $\vec{F}$ is the external body forces, respectively. In this work, the gravitation term and the external forces are ignored.

4) Energy conservation

$$\frac{\partial(\rho E)}{\partial t} + \nabla \cdot (u(\rho E + p)) = -\nabla \cdot \left(\lambda \nabla T - \sum_i h_{s,i}\vec{J}_i + \tau \cdot u\right) + \dot{w}_T + S_h + S_{\vec{F}}, \quad (3\text{-}4)$$

where E is the energies expressed by

$$E = h_s - \frac{p}{\rho} + \frac{u^2}{2}, \quad (3\text{-}5)$$

wher h_s is the sum of the species enthalpy

$$h_s = \sum_i h_{s,i}. \quad (3\text{-}6)$$

p is the pressure, λ is the effective conductivity, $\dot{w}_T$ is the heat released by the combustion, S_h is the heat sources other than the combustion heat.

5) State equation

For the compressible ideal gas, the state equation of pressure p, density ρ and temperature T is

$$p = \rho RT \quad (3\text{-}6)$$

where R is the specific gas constant.

3.2.4. Chemistry model

The methane/air reaction is complicated and involves dozens of reactions and hundreds of elementary reactions. Several reaction mechanisms have been proposed to accurately describe the combustion process. The detailed reaction mechanisms are highly precise [62], while the computational costs are increased. In a numerical comparison between the different methane/air combustion mechanisms, Li [63] pointed out that the one-step

mechanism agrees with experimental results quantitatively for fuel-lean conditions. Acampora et al. [64] concluded that moving from a one-step global mechanism to a two-step mechanism does not significantly increase the accuracy of predictions. According to the mentioned points, the one-step reaction mechanism is used for the reaction of methane and air and is expressed as

$$CH_4 + 2(O_2 + 3.76N_2) \overset{K_G}{\rightarrow} CO_2 + 2H_2O + 7.52N_2 \quad (3\text{-}7)$$

The rate of reaction is given by the global Arrhenius equation as:

$$\frac{\mathrm{d}[CH_4]}{\mathrm{dt}} = -Aexp\left(\frac{-E_a}{R_uT}\right)[CH_4]^m[O_2]^n \quad (3\text{-}8)$$

Where the parameter A, E_a/R_u, m and n are given in Table 3-2 [65]-[66].

Table 3-2 Parameters of the chemistry model for methane and air reaction

Pre-exponential factor A $\left[(\mathrm{kmol/m^3})^{(1-m-n)}/\mathrm{s}\right]$	Activation Temperature Ea/Ru [K]	m	n
2.119×10^{11}	24,379	0.2	0.3

3.2.5. Radiation model

Due to the high temperatures of the flame, radiative heat transfer becomes one of the dominant mechanisms of heat transfer in addition to conduction and convection heat transfer [67]-[68]. Hence, proper simulation of the radiative heat transfer is of great importance to this problem. The P-1 model is based on the expansion of the radiation intensity *I* into an orthogonal series of spherical harmonics and has high accuracy and the ability to consider the radiation exchange in the flame environment [70]-[72]. For this advantage, the P-1 model is widely used in the simulation of combustion [73]-[74]. In this work, the P-1 radiation model was chosen to model the high-temperature flow problem.

The radiation flux term in the energy balance is as following

$$-\nabla \cdot q_r = \sigma\kappa - 4\sigma\Upsilon^2\sigma T^4. \quad (3\text{-}9)$$

Where σ, κ, Υ, and σ are the absorption coefficient, the incident radiation, the refractive index of the medium and the Stefan-Boltzmann constant, respectively.

3.2.6. The CFD method

The governing equations are solved with the finite-volume method. The average velocity at steady state is approximately 0.026 m/s, the corresponding Reynolds number is approximately 120, and the Mach number is 1.5×10^{-4} in this model, indicating that this is a laminar flow for the non-reacting condition. The species is determined by the species transport model, while the finite-rate model is applied to compute chemistry reaction. The material properties used in the simulation are listed in Table 3-3.

Table 3-3. Material properties for the Rijke burner simulation

Material	Properties	Unit	Parameter setting
Fuel-air mixture	Density	kg/m^3	Ideal gas
	Specific heat (Cp)	J/(kg·K)	Mixing law
	Thermal conductivity	W/(m·K)	Ideal gas mixing law
	Viscosity	kg/(ms)	Ideal gas mixing law
	Mass diffusivity	m^2/s	Kinetic-theory
	Thermal diffusion coeff.	kg/(ms)	Kinetic-theory
	Reaction		One-step finite-rate reaction
	Radiation		P-1
Tube wall	Material		Carbon steel
	Height	mm	1572
	Inner diameter	mm	73.7
	Wall thickness	mm	7.62
	Density	kg/m^3	8030.0
	Thermal conductivity	W/(m·K)	16.27
	Specific heat (Cp)	J/(kg·K)	502.48
Flame stabilizer	Material		Cordierite
	Thickness	mm	25.4
	Diameter	mm	73.7

Density	kg/m^3	2300
Thermal conductivity	W/(m·K)	2.28228
Specific heat (Cp)	J/(kg·K)	850.63
Area restriction		50%

The first difficulty in the simulation of combustion flow is that the flame reaction happens on a very thin surface, which has been solved by the hybrid grid scheme. Now we are still facing another two challenges. One is the different time scales in flow field, acoustic, and reaction, and this issue makes the computation of species transport equation difficult. Another issue is that the strong coupling of combustion, flow, and acoustics is nonlinear. This high nonlinearity makes the computation high sensitive to the computing parameters and high probability of diverging during the simulation.

A two-step scheme is used in this work to overcome the above two challenges. First, a clod non-reacting flow field is simulated, then the steady-state reacting flow is ignited by patching 2000 K high temperature at the flame region in Figure 3-3. The second step is the simulation of self-excited combustion instability. The second-order implicit formulation in spatial discretization. The pressure implicit with splitting of operators (PISO) scheme has been applied. The under-relaxation factors for the species and energy are initially set to 0.1 and are gradually increased to 0.9 to prevent divergence.

The initial condition of transient simulation is set as the steady-state results. The time step is set to 1×10^{-5} s to capture the dynamic of reaction.

The initial conditions of the two steps are listed in Table 3-4.

Table 3-4. Initial conditions for the two-step simulation scheme of Rijke burner

Simulation step	Initial condition
Step 1:Steady-state reacting flow simulation	The inlet parameter
Step 2: Unsteady reacting flow simulation	The result of the steady-state solution

3.2.7. Grid independence and model verification

To verify the computational model and grid independence, the numerical results of the axial temperature distribution at the centerline under steady-state combustion are

compared. Three different numbers of nodes, namely, 26312, 67056, and 195233 nodes, are compared with the previous numerical modeling of Wang [24], and the results are presented in. The convergence limit is assumed when the residual values are less than 10^{-6}.

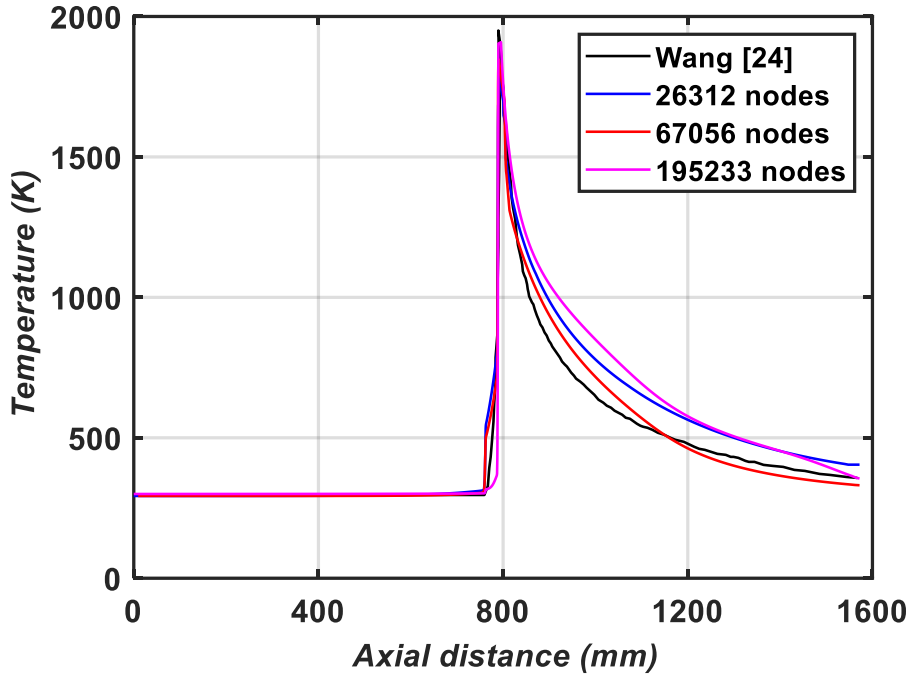

Figure 3-4. Comparison of the grid independence solutions of axial temperature.

As shown in Figure 3-4, the temperature distributions before the flame stabilizer almost converge to the same value, while in the flame stabilizer area and after the flame zone, the temperature increases sharply because of the heat released by the flame. The result of the 67056-node scheme is closer to the result presented by Wang [24] than the other two grid schemes.

The peak temperatures of the computational grids with 26312, 67056, and 195233 nodes are approximately 1804 K, 1847 K, and 1908 K, respectively, and the outlet temperatures are 408 K, 331 K, and 354 K, while the peak temperature and outlet temperature in Wang's simulation are 1927 K and 320K, respectively. In addition, for the outlet temperature, the result of the 67056-node scheme is much closer to the result of Wang. Consequently, the mesh with 67056 nodes was selected as the best computation grid for computational modeling.

3.3. Steady-state solution

The modeling of thermoacoustic instability proceeds in two steps—the first step is the simulation of the steady-state reacting flow, and the second step is the simulation of the transient reacting flow. For the steady-steady reaction simulation, the flow field was initialized with the inlet parameters.

The solution of the steady-state reacting flow includes the accurate capture of the flame anchoring process shown in Figure 3-5, the steady-state temperature distribution along the combustor shown in 3-6, and the consumption of reactants and product formation shown in Figure 3-7. Each process/distribution is vital for the verification of the computational results against the theoretical and experimental results.

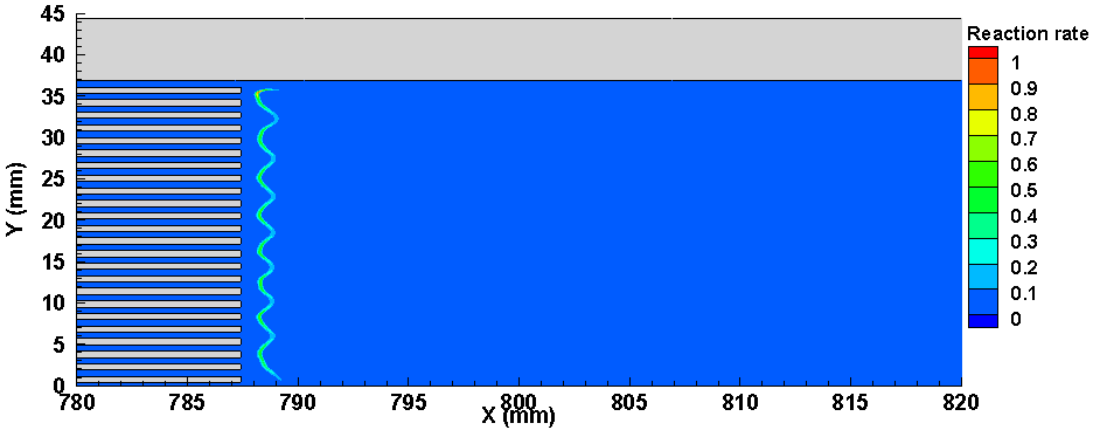

Figure 3-5. Reaction rate [kmol/m^3·s] contour plots of the flame stabilizer channels and flame zone.

The reaction rate and temperature contour plots downstream of the flame stabilizer are shown in Figure 3-5 and 3-6, in which the location of the highest reaction rate and the highest temperature indicate the flame location. As seen in the figures, the flame sits just on the outlet of the flame stabilizer at a distance of 1-2 mm away from it. The temperature contours show that the incoming flow is preheated to approximately 800 K at the outlet of the honeycomb and then heated to a peak temperature of 1828 K by the reaction. Then, a steep temperature gradient, which is dominated by radiation heat transfer, occurs downstream of the peak temperature point. With decreasing

temperature, the influence of radiation weakens, and the temperature gradient becomes increasingly gentle until the flow reaches the outlet.

The mass fractions of reactants and products along the centerline in the flame stabilizer area and the flame zone are shown in Figure 3-7. Due to the preheating effect of the flame stabilizer and flame radiation, the reaction starts before the flame stabilizer outlet and rapidly increases to a peak downstream of it. At the flame location, the reaction rate reaches its maximum value, the CH_4 fuel is completely consumed, and its mass fraction becomes zero. The steady-state species distribution and kinetic reaction rate show the exact location of the flame and demonstrate the effectiveness of the numerical simulation in this work.

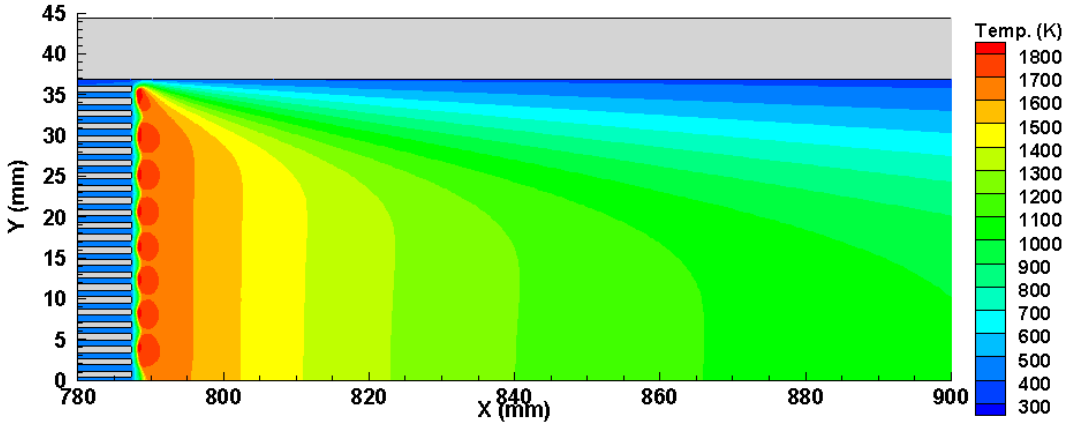

Figure 3-6. Temperature contour plots of the flame stabilizer channels and flame zone.

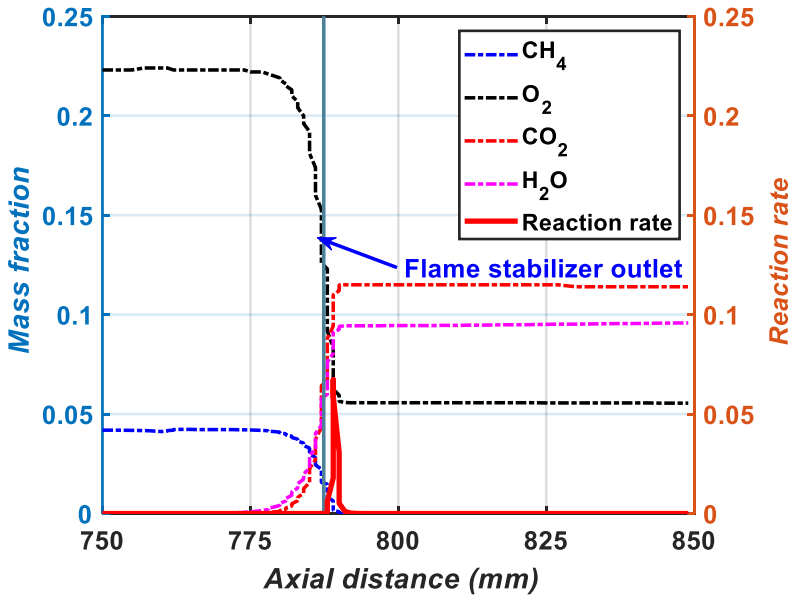

Figure 3-7 Species mass fraction distribution and reaction rate [kmol/m^3·s] along the centerline.

In addition, the average flow velocity in the tube of the cold flow and steady-state reacting flow is obtained. The results show that the average velocity increases from 0.0257 m/s to 0.071 m/s because the heat released from the flame heats and expands the flow.

3.4. Self-excited pressure oscillation

3.4.1. the exponential growth of combustion instability

To capture the dynamic characteristics of thermoacoustic insatiability, a transient simulation is conducted. Here, the steady-state reacting flow field is set as the initial condition of the dynamic flow. The time step is set to between 1×10^{-5} s and 1×10^{-4} s to obtain enough information in the time domain while meeting the convergent requirements in previous research [26],[27],[75]; here, it is set to 1×10^{-5} s. The transient solution includes the growth of the self-excited instability, the subsequent limit cycle behavior of pressure and velocity, the oscillating frequencies and modes, and the periodic behavior of the flow field.

The instability growth mechanism is characterized by increasing oscillations of pressure inside the combustor. Figure 3-8(a) shows the time evolutions of average pressure and average velocity 5 cm downstream of the flame stabilizer. Figure 3-8(b) shows the growth of total reaction heat released by the flame. The steady-state value of pressure, velocity, and heat release are 0 Pa, 0.1226 m/s, and 63.68 W, respectively. Approximately 0.05 s after the time integration is initialized, the pressure, velocity, and reaction heat start to increase exponentially. The oscillation grows until approximately 0.86 s and reaches maximum amplitudes. After several periods of amplitude adjustment from 0.86s to 1.1s, the system reaches a 'saturated' state, which is referred to as the limit cycle state. The pressure, velocity, and reaction heat maintain at amplitudes of approximately 208 Pa, 0.39 m/s, and 10.79W, respectively.

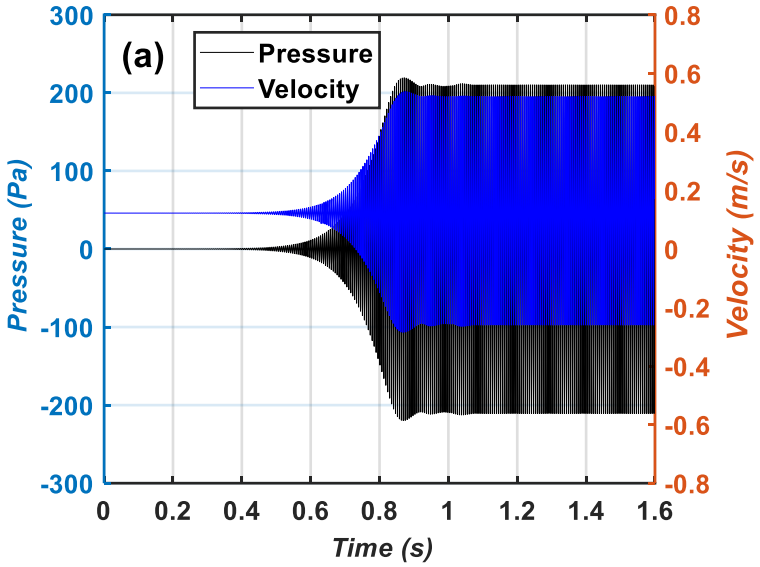
(a)
Pressure
Velocity
Pressure (Pa)
Velocity (m/s)
Time (s)

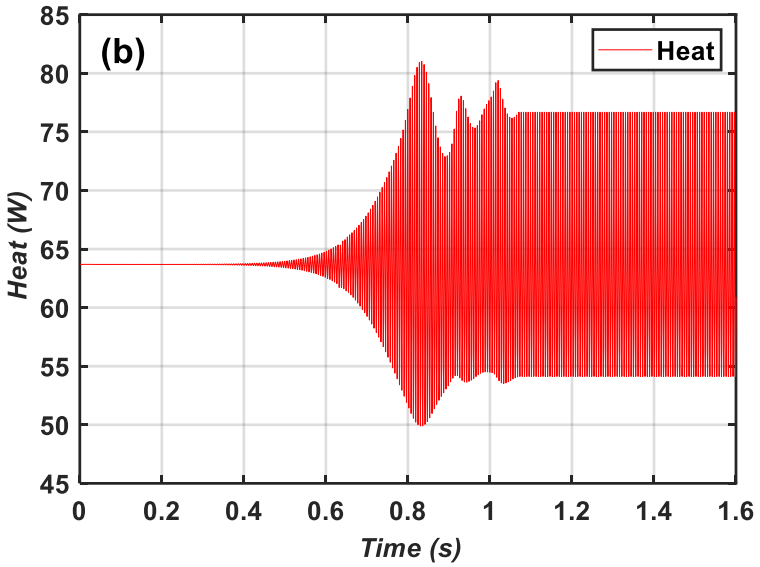
(b)
Heat
Heat (W)
Time (s)

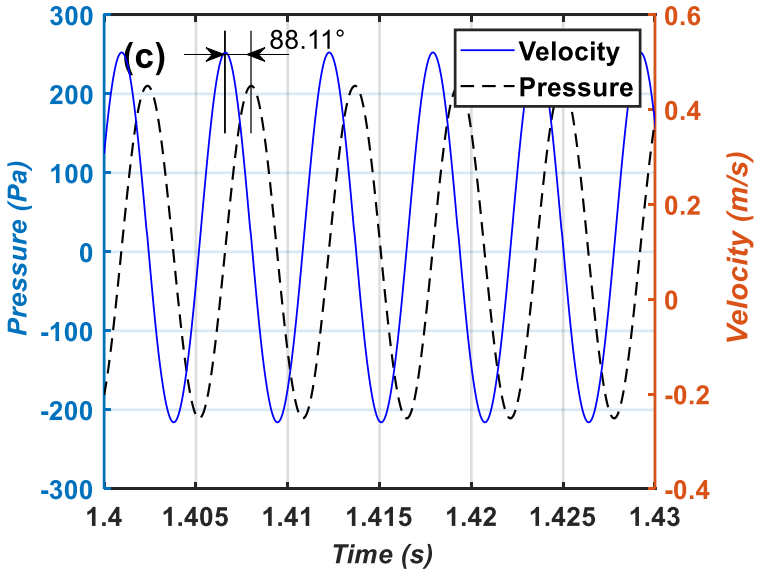
(c)
88.11°
Velocity
Pressure
Pressure (Pa)
Velocity (m/s)
Time (s)

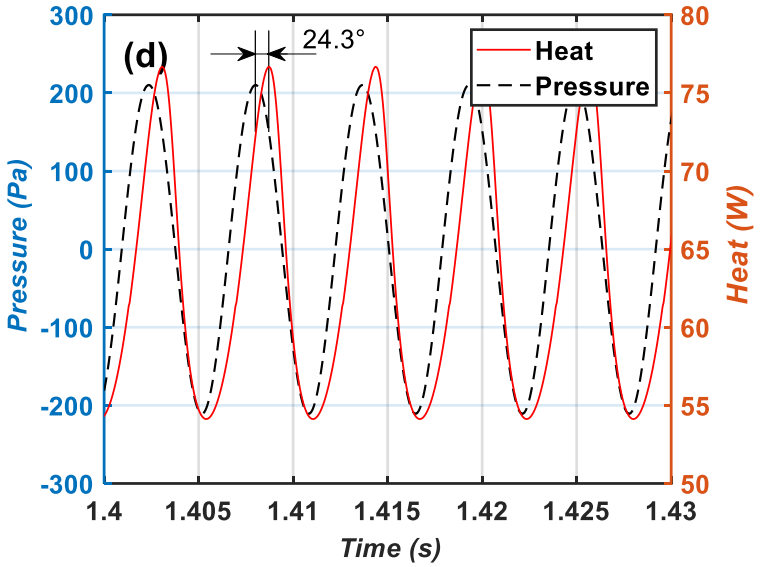

Figure 3-8. The time evolutions of pressure, velocity, and heat release of the flame

Figure 3-8(c) illustrated the phase relationship between the average pressure and velocity 5 cm downstream of the flame stabilizer at the limit cycle oscillation state. it can be seen that the velocity has a 88.1° phase advance relative to the pressure.

Figure 3-8(d) illustrated the phase relationship between the average pressure 5 cm downstream of the flame stabilizer and total heat release of the flame at the limit cycle oscillation state. The results show that the reaction heat release has a 24.3° phase delay relative to the pressure, which fulfills the Rayleigh Criterion that oscillations are encouraged when heat fluctuates in phase with pressure perturbation [15]. It can be calculated that the reaction heat has a 114.34° phase delay relative to the velocity. This time delay between reaction heat and velocity has been proved to be a critical role in the stability of the Rijke type thermoacoustic system [23].

Two important parameters to evaluate the growth of thermoacoustic instability are the growth rate of the acoustic disturbances α and G. The definition and detail derivation of α and G can be found in the reference [76], Where, α is the predicted maximum growth rate of the acoustic disturbances, and G is the normalized maximum growth rate. For the premixed air and methane mixture, the specific heat ratio can be set as γ=1.4 since the mass fraction of air is an overwhelming majority, there is a maximum possible

growth rate G_{max}=9.2 × 10^{-2} rad/s^2.

The time evolution of the pressure and heat release of the flame from 0 s to 0.4 s are illustrated in Figure 3-9 and Figure 3-10. It can be seen that both the pressure and heat release are growing exponentially after an adjustment of about 0.05 s. Two exponential functions are constructed to fit best the series of local maximum and minimum points in Figure 3-9 and Figure 3-10, and they are written as:

$$\tilde{p} = \pm Ae^{\alpha_1 t} + B \tag{3-10}$$

$$\widetilde{W} = \pm Ce^{\alpha_2 t} + D. \tag{3-11}$$

where $\tilde{p}$ is the series of local maximum and minimum pressure, $\widetilde{W}$ is the series of local maximum and minimum reaction heat, A, B, C, D, α_1, α_2 and β are parameters to be solved.

The equations (3-4) and (3-5) are solved by iteration, getting the growth rate α_1 is 13.77 s^{-1}, α_2 is 13.85 s^{-1}, corresponding to a calculated G_{cal} is 1.22 × 10^{-2} rad/s^2, which is within the range of maximum possible growth rate for this type of combustion-driven acoustic disturbances, G_{max}=9.2 × 10^{-2} rad/s^2. The different between G_{cal} and G_{max} is caused by acoustic damping and boundary losses.

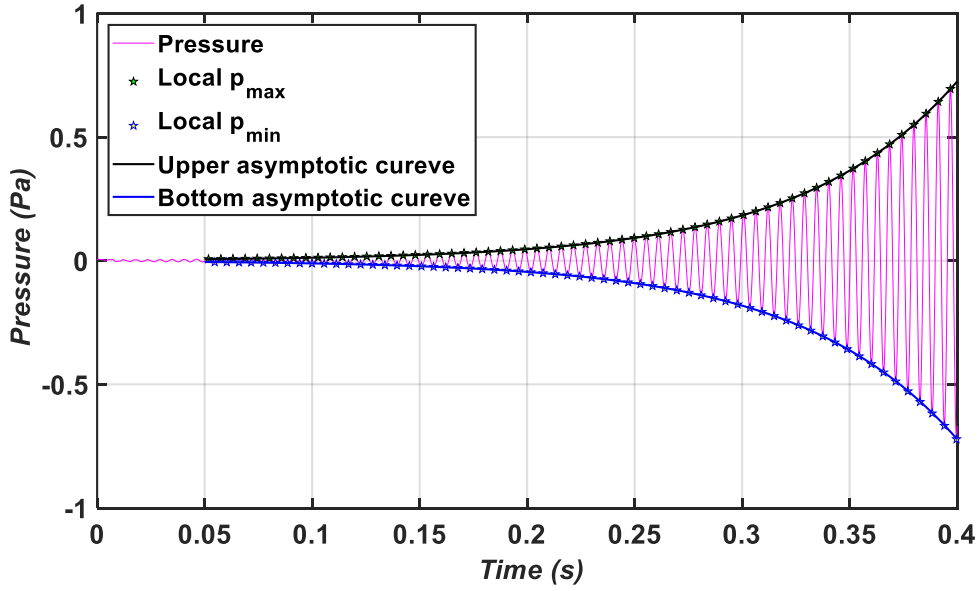

Figure 3-9 Time evolution of the pressure disturbances and the growth rate fitting curve

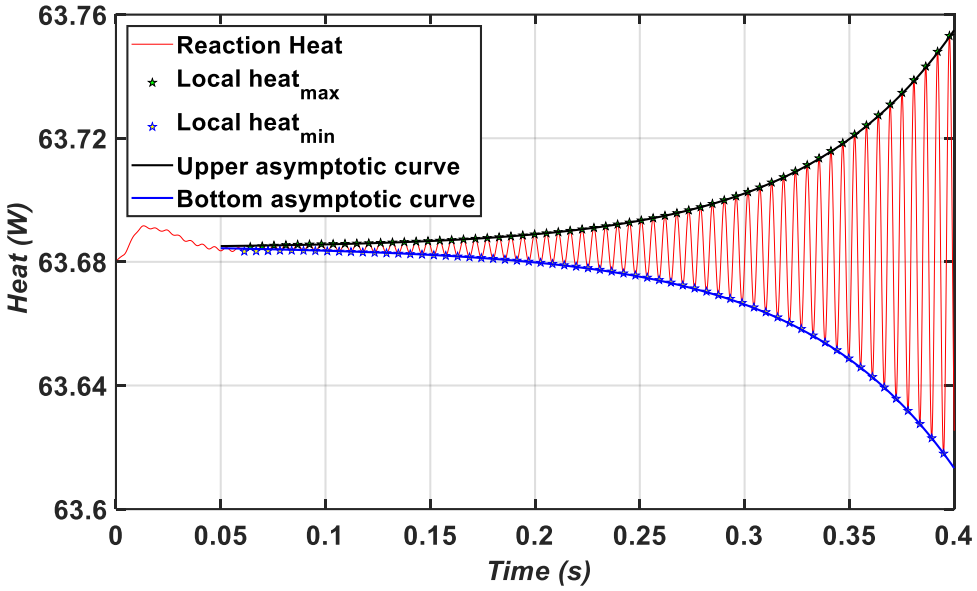

Figure 3-10 Time evolution of the unsteady heat release and the growth rate fitting curve

3.4.2. The limit cycle oscillation

From the analysis of Yoon et al.[21], the analytic pressure modes and velocity models of the acoustic perturbation for the acoustically closed-open Rijke-type burner can be expressed by Eqs. (3-6) and (3-7):

$$P_n = \cos((2n-1)\,\pi x/2\mathrm{L}) \quad n = 1,2,3\cdots\infty \tag{3-12}$$

$$V_n = \sin((2n-1)\,\pi x/2\mathrm{L}) \quad n = 1,2,3\cdots\infty \tag{3-13}$$

and the corresponding acoustic frequencies can be calculated by:

$$f_n = \frac{2n-1}{4L}a \quad n = 1,2,3\cdots\infty \tag{3-14}$$

where f_n is the n-th acoustic frequency, and a is the sound speed.

According to the Rayleigh criterion, oscillations are encouraged when heat fluctuates in phase with pressure perturbation. This system hasn't the first frequency, since for n=1, the f_n and V_n is 0, implying there will be no oscillation. It can be determined from Eq. (3-12) that the second acoustic mode may be excited when the unsteady heat is located at the center of the tube length because the flame is near the antinode of the second acoustic mode, which has a three-quarter wave mode shape. The frequency of this mode

is 168.8 Hz with the inlet parameter by solving Eq. (3-4).

The frequency component of simulated pressure oscillation from 1.4 s to 1.6 s is calculated and displayed in Figure 3-11. The excited frequency is 179 Hz, which is 6% higher than the predicted acoustic frequency of 168.8 Hz for the non-reacting flow. The slight discrepancy is due to the flow in the tube being heated by the flame, which induces an increase in the sound speed. Furthermore, the increased sound speed results in an increase in the oscillation frequency. Thus, researchers should take the frequency increase effect into consideration when predicting the thermoacoustic instability frequency with the inlet parameters.

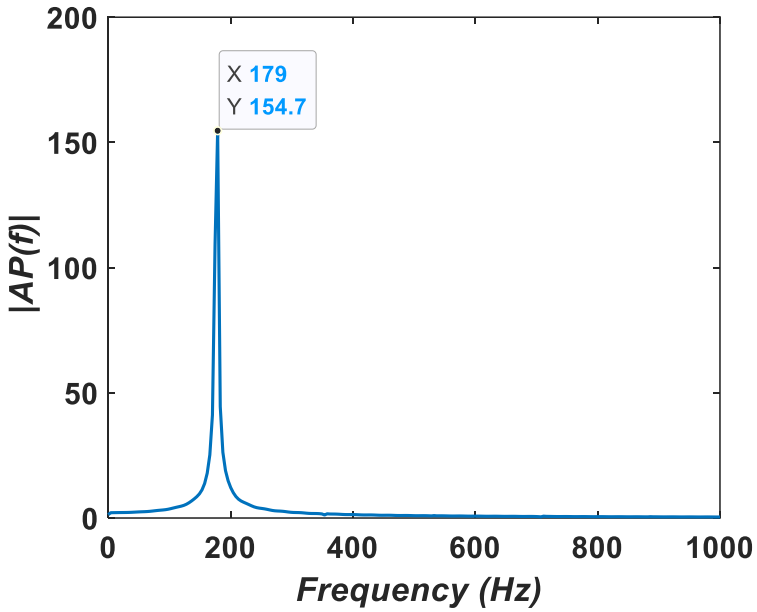

Figure 3-11. FFT plot of the gauge pressure.

To compare the simulated oscillating mode with the prediction, the dynamic pressure along the centerline at time 1.400445 s is normalized by the maximum pressure amplitude. Meanwhile, the velocity along the centerline at time 1.40585 s is normalized by the maximum velocity amplitude. In Figure 3-12, the normalized pressure and axial velocity of this work are compared with the analytical second acoustic pressure mode and velocity mode, and the normalized pressure and axial velocity in reference [21]. The simulation pressure distribution along the centerline is in good agreement with the

analytical results and the results of Wang. While for the velocity distribution, two areas appear to have significant differences between the numerical results and the analytic results. The first area is in the flame stabilizer, where the simulated velocity is two times the analytical velocity because the flame stabilizer occupies half of the total volume of the entire flame stabilizer zone. The other inconsistent area is on the outlet face because it is set as a pressure outlet, and the mass flow in the tube must be conserved. To further study this problem, it will be better to impose constraints on the velocity derivative on the outlet boundary. Aside from these two areas, the simulated velocity distribution agrees with the prediction results.

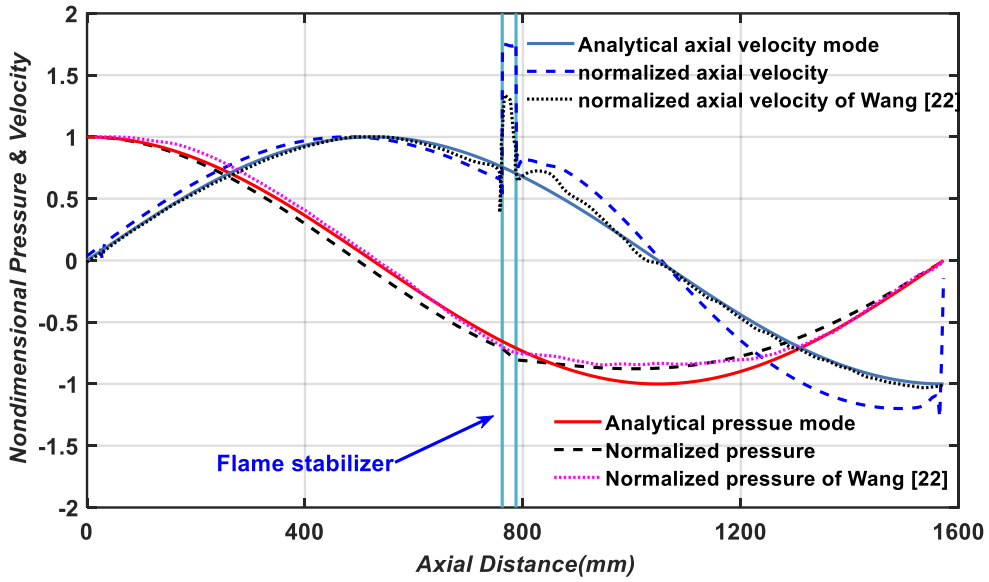

Figure 3-12. Comparison of the simulated pressure and velocity along the centerline with the analytical prediction results.

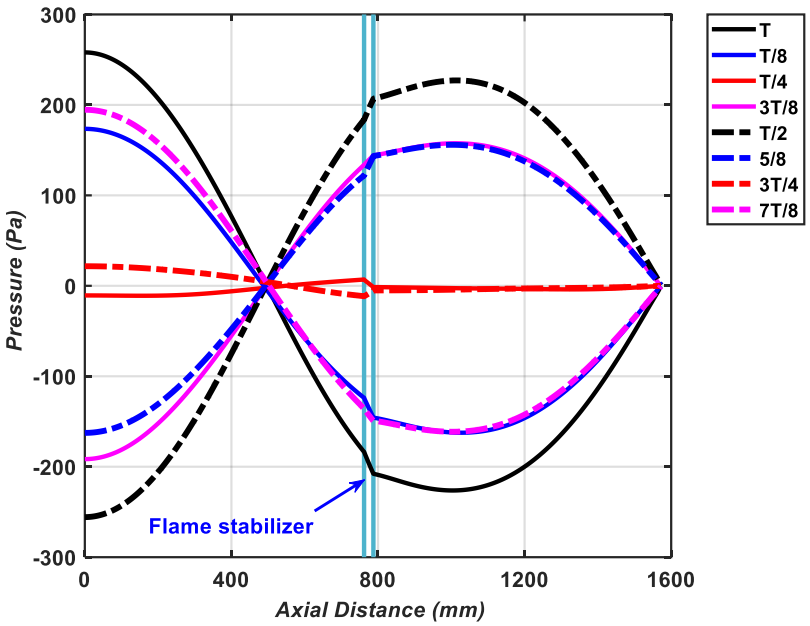

Figure 3-13. Pressure distribution along the centerline at different times of a limit cycle [Pa]

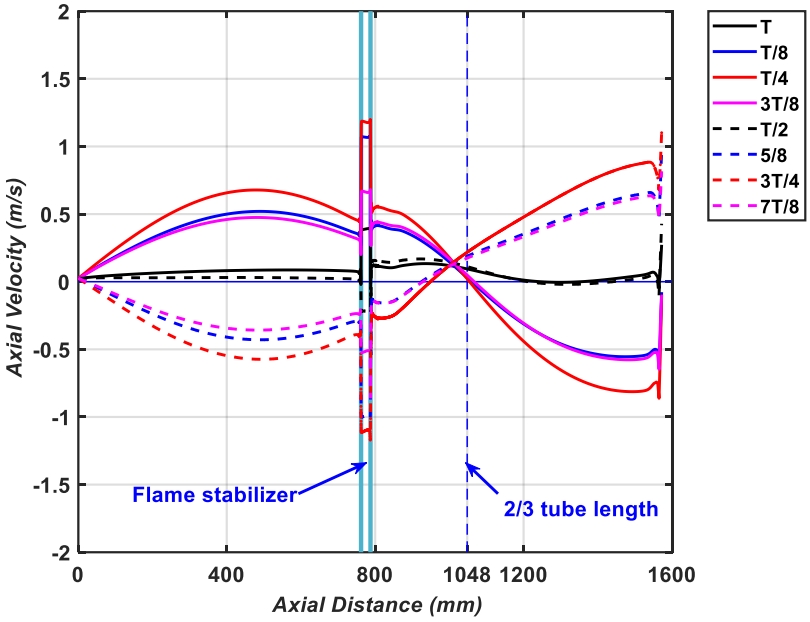

Figure 3-14. Axial velocity distribution along the centerline at different times of a limit cycle.

Figure 3-13 and Figure 3-14 show the instantaneous axial pressure distribution and axial velocity along the centerline of the Rijke burner at eight different times of a limit cycle, namely, at times T, T/8, T/4, 3T/8, T/2, 5T/8, 3T/4, and 7T/8. In Figure 3-13, it can be seen that the pressure node point is at 1/3 length, and the pressure antinode point occurs downstream of the flame stabilizer at approximately 2/3 length, which matches the theoretical pressure maximum location for a three-quarter wave shown in Figure 3-12.

From Figure 3-14, one can see that the velocity node point occurs slightly before the 2/3 tube length, which is also the pressure summit point of the pressure distribution.

3.4.3. The unsteady flow field in the limit cycle state

Here, the flow field within one cycle is analyzed. As shown in Figure 3-15, the dynamic pressure and velocity of a cycle is presented. The flow field of 20 typical transients marked in Figure 3-15 will be analyzed later in Figure 3-17. The instant t=1.4009 when pressure is zero is marked as the time T0, and the instant t=1.40665 when the is marked as the time T0+T. and all the other instants during this period can be calculated by

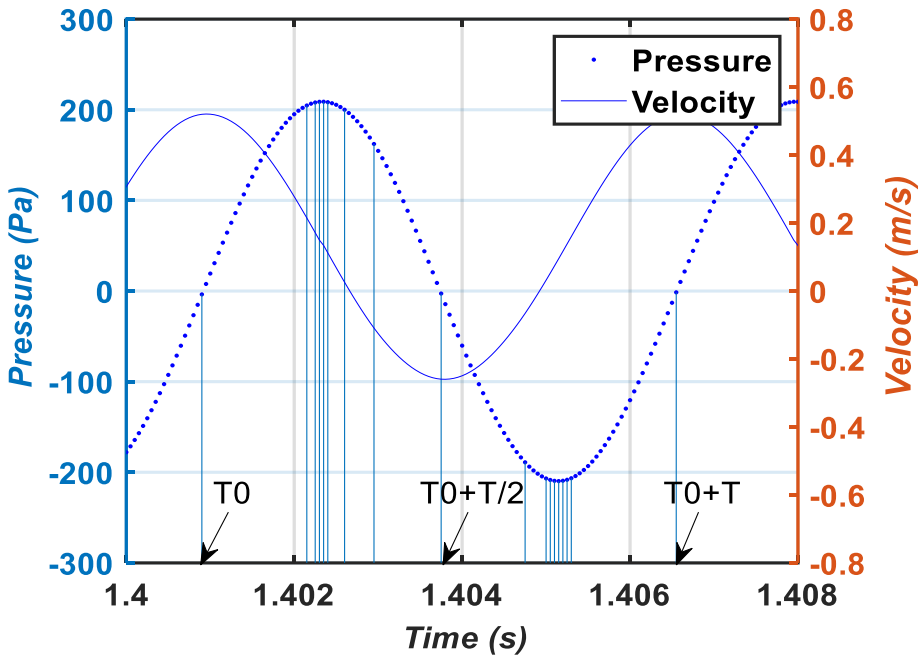

Figure 3-15. Evolution of pressure and axial velocity in an oscillating cycle.

The instantly axial velocity contour of time T0+T/2 is shown in Figure 3-16, from which we can see that there is negative flow in the flame area. Referring to the velocity measured 5 cm downstream of the flame stabilizer showing in Figure 3-15, we can conclude that for the case studied in this work, there is backflow occurring in the flame zone. This is an unwanted phenomenon because it may cause a flame flashback or even flameout.

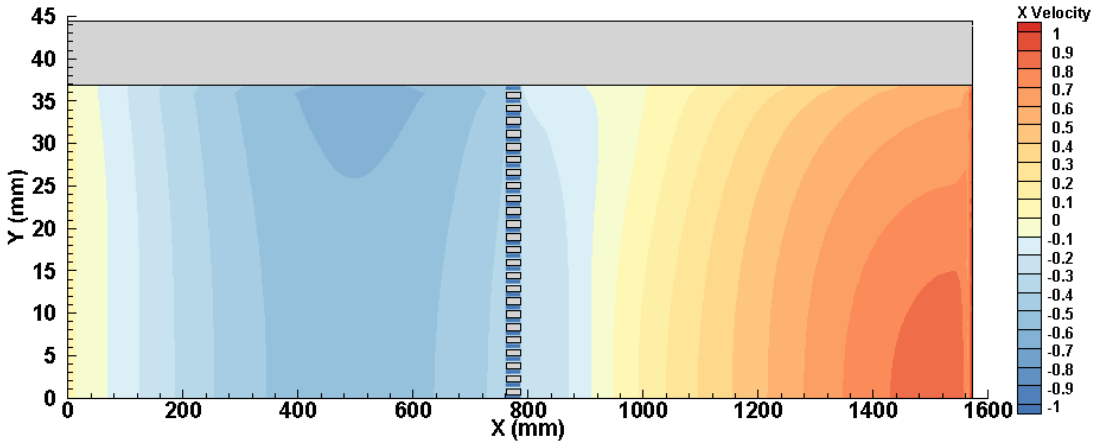

Figure 3-16. The negative axial velocity in the flame area.

Figure 3-17 illustrates the axial velocity distribution and streamline at different times within a period of one limit cycle, where the yellow regions represent velocities above zero, the blue regions represent velocities below zero, and the gray regions represent the solid zone. Once the system is excited into the periodical oscillating state, the flow in the tube does not remain steady and uniform; instead, it begins oscillating back and forth. The starting of a cycle is chosen at the transient T0 that the dynamic pressure is zero, since the velocity 88.1° phase advance relative to the pressure, thus at this time, the axial velocity nearly reaches its maximum.

At the beginning of a period, the velocity is positive in the left 2/3 of the tube length and negative in the right 1/3 of the tube length, as shown in Figure 3-17 (a). At approximately 2/3 of the tube length, which is a node point of the velocity mode in the 1-D analysis, the axis velocity is zero. This result is in good agreement with the predicted velocity mode, and the velocity along the axis is in agreement with the velocity at time T0 in Figure 3-15.

As time goes on, the value of axial velocity in the flame zone decrease, but it is still positive. Thus the positive velocity area expands to the right direction. Due to the existents of the boundary layer, the velocity fluctuation near the tube wall is smaller than that in the mainstream zone. This inconsistency of relative speed makes the movement range of zero-velocity points near the tube wall is smaller than that of the

mainstream zone, as shown in Figure 3-17 (b).

In the flame zone, due to the influence of the high-temperature flame, the flow is compressed and distorted, inducing the formation of a clockwise vortex after the flame area, as shown in Figure 3-17 (c), then the positive velocity fluid flows into the right 1/3 tube. As the growth of this clockwise vortex, a counterclockwise vortex is formed at the inner wall of the left half of the tube in Figure 3-17 (d). At transients T0+T/4, These vortices are enlarged and change the direction of flow in Figure 3-17 (e). They occupy the most flow path of the left half tube and make the flow negative on the left half of the tube length, as shown in Figure 3-17 (f). The negative velocity area is getting larger with time, as shown in Figure 3-17 (g) and (h). Until T+T/2, the flow becomes negative on the left 2/3 of the tube length and positive on the right of the 1/3 tube length, as shown in Figure 3-17 (i), and the velocity reaches a minimum in Figure 3-15.

After time T+T/2, the velocity begins to increase from its minimum value, and the negative flow area is minified in Figure 3-17 (j) and Figure 3-17 (k), compared with Figure 3-17 (i). With time, the flow is compressed near the inlet face and is expanded in the flame zone. When the negative flow is heated by the flame, followed by the formation of new vortices show in Figure 3-17 (l), and the subsequent development and collapse of these new vortices as shown in Figure 3-17 (m), (n), (o), and (p). in Figure 3-17 (q), all the vortices have vanished. Meanwhile, the direction of flow changes as the left 2/3 is positive and the right 1/3 is negative, then flow in the after the flame area is compressed until time T0+T shown in Figure 3-17 (r), A new period begins.

The flow field variation in a limit cycle shown in Figure 3-17 demonstrates that vortices emerge and vanish when thermoacoustic instability occurs, Especially in the range of (T0+0.221T, T0+0.256T), the neighborhood of transient T0+T/4, and (T0+0.717T, T0+0.77T), which are in the neighborhood of transient T0+3T/4, the flow field varying in a large amplitude with twisting and rolling up of the streamlines.

(a) t=1.40090 =T0	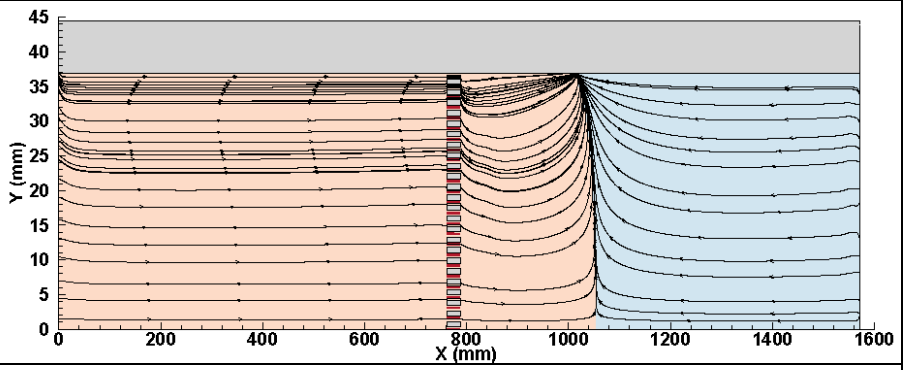
(b) t=1.40215	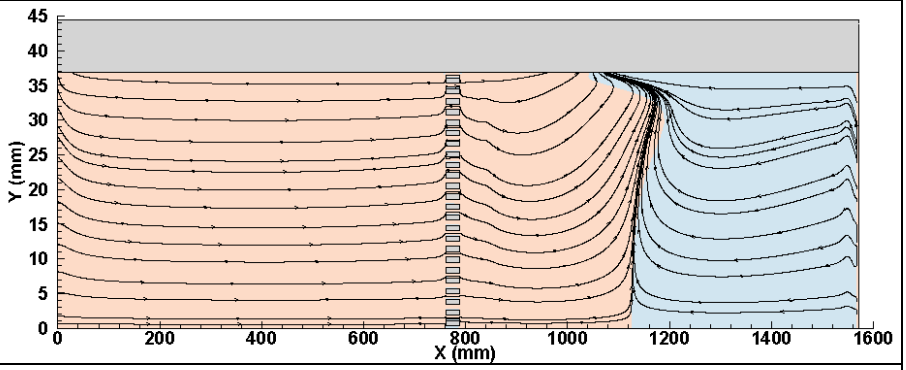
(c) t=1.40225 =T0+0.221T	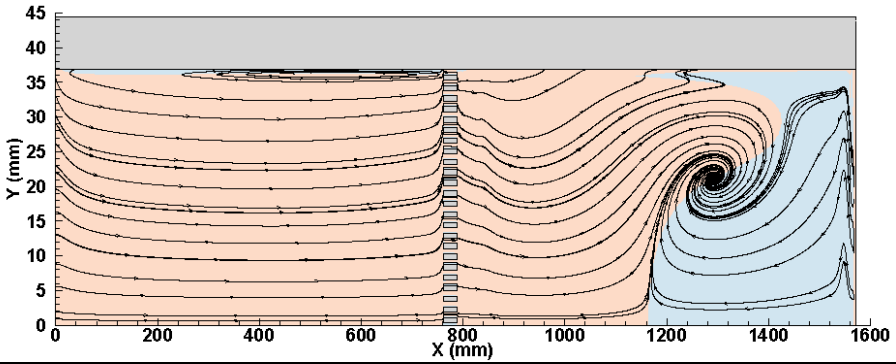
(d) t=1.40230	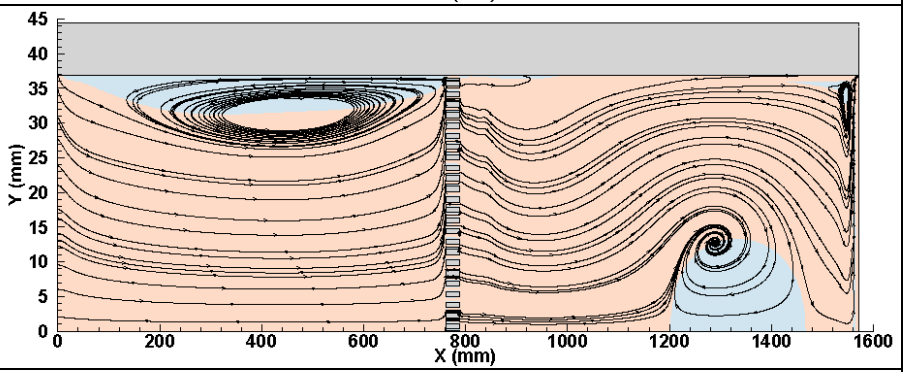
(e) t=1.40235 =T0+T/4	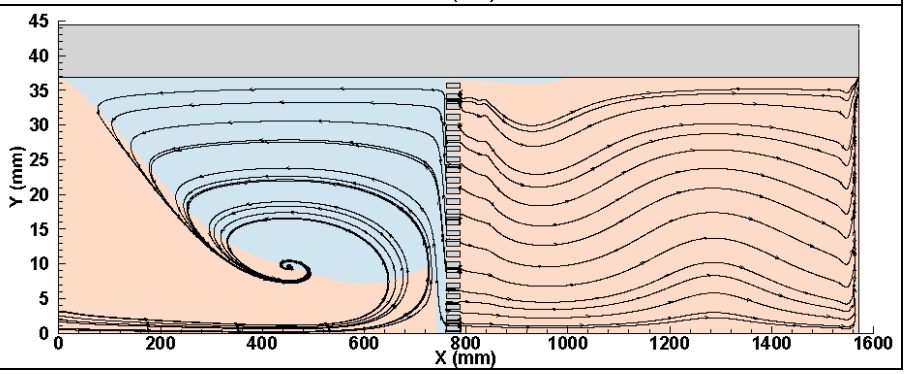

(f) t=1.40240 =T0+0.256T	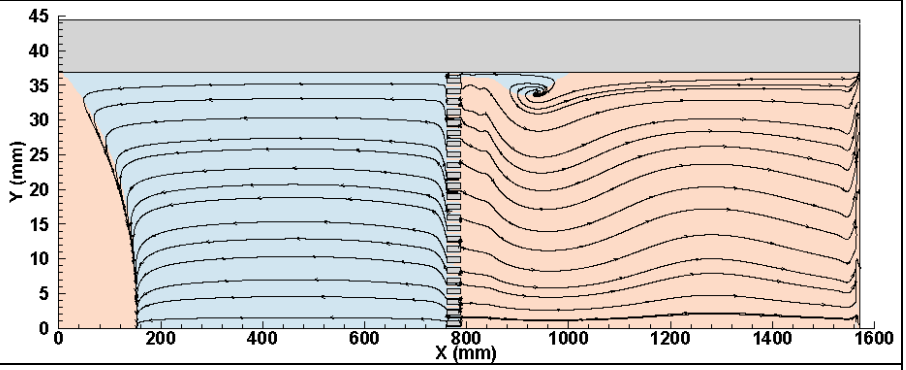
(g) t=1.40260	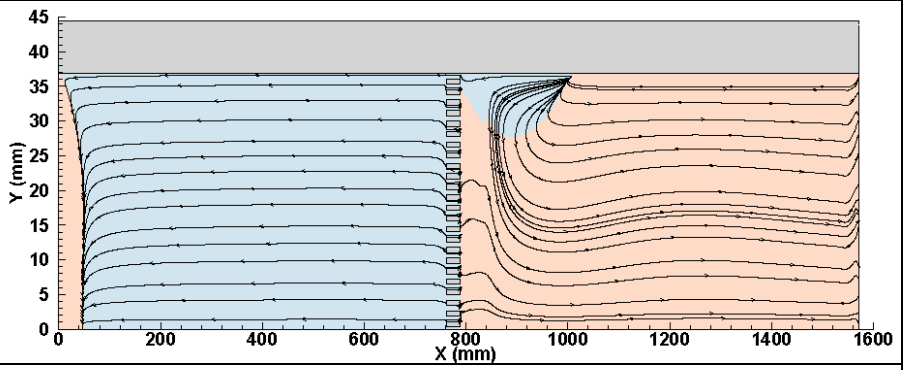
(h) t=1.40295	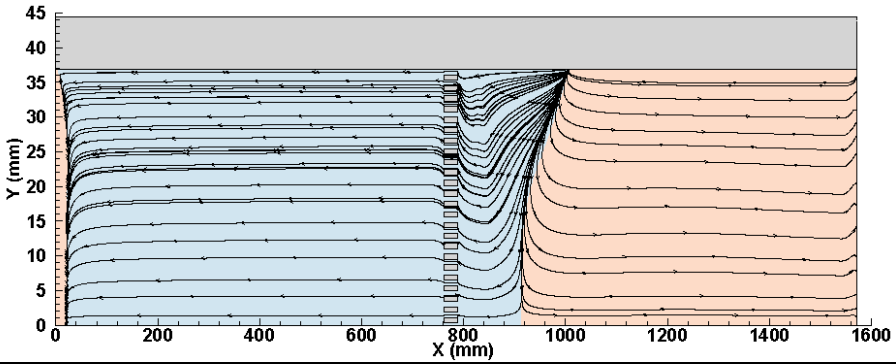
(i) t=1.40375 =T0+T/2	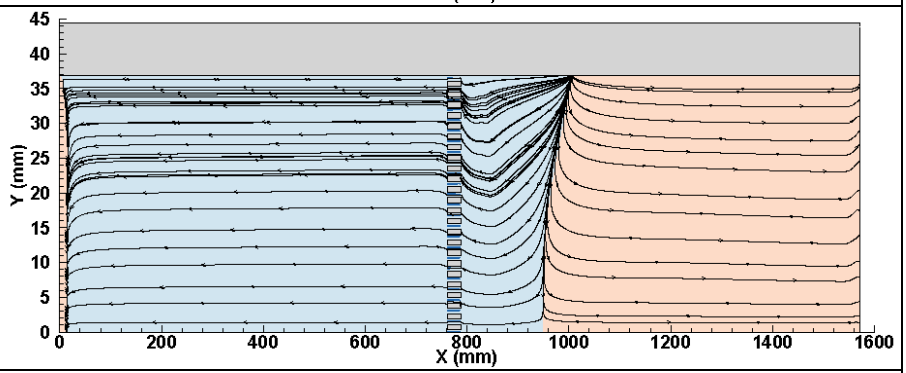
(j) t=1.40475	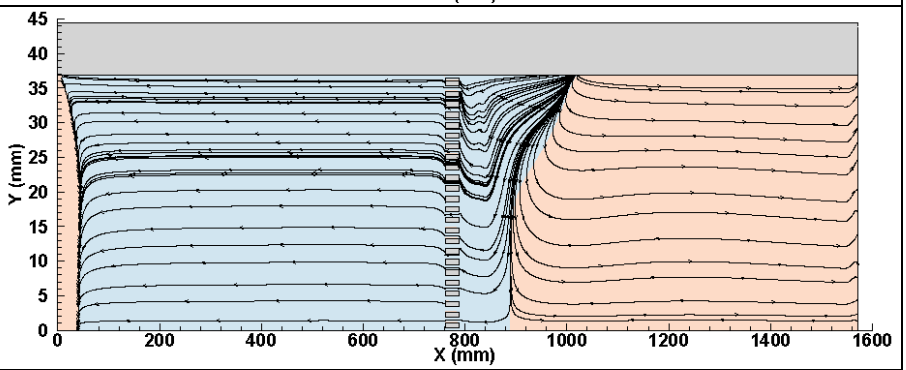

(k) t=1.40500 =T0+0.717T	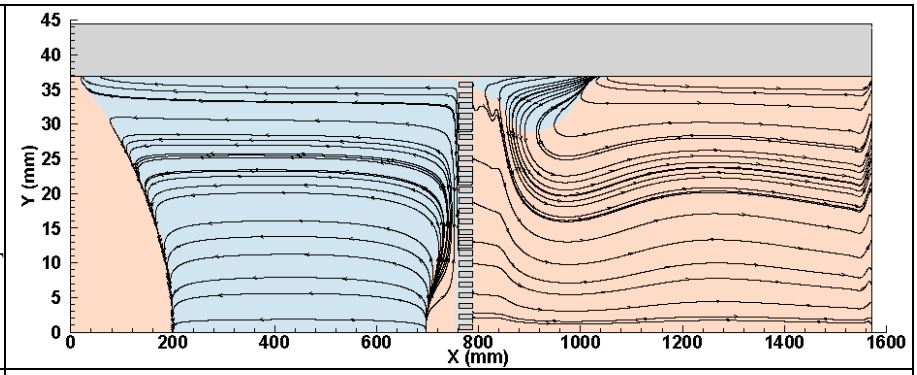
(l) t=1.40505	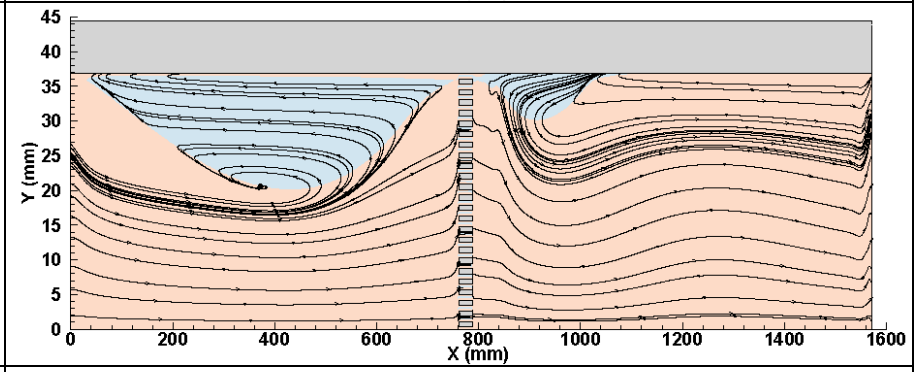
(m) t=1.4051	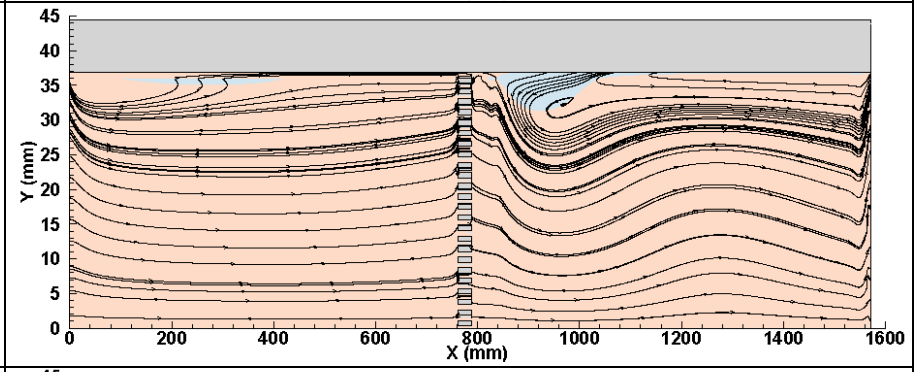
(n) T=1.40515	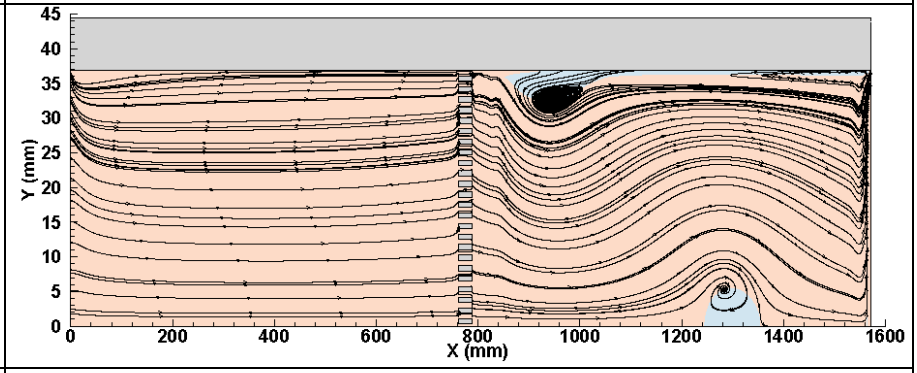
(o) t=1.40520 =T0+3T/4	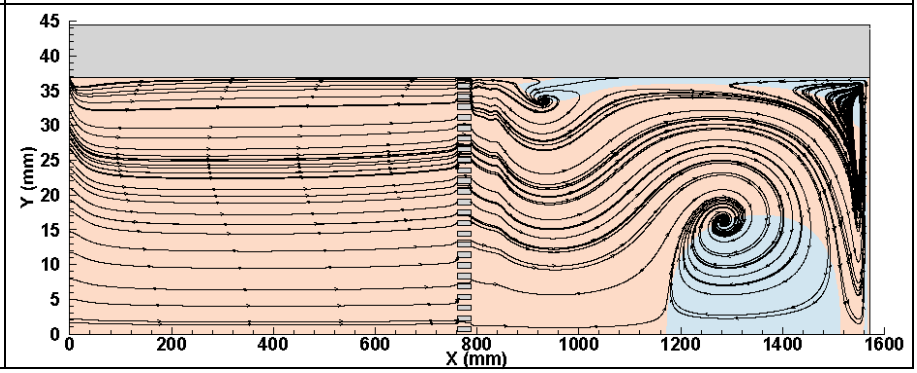

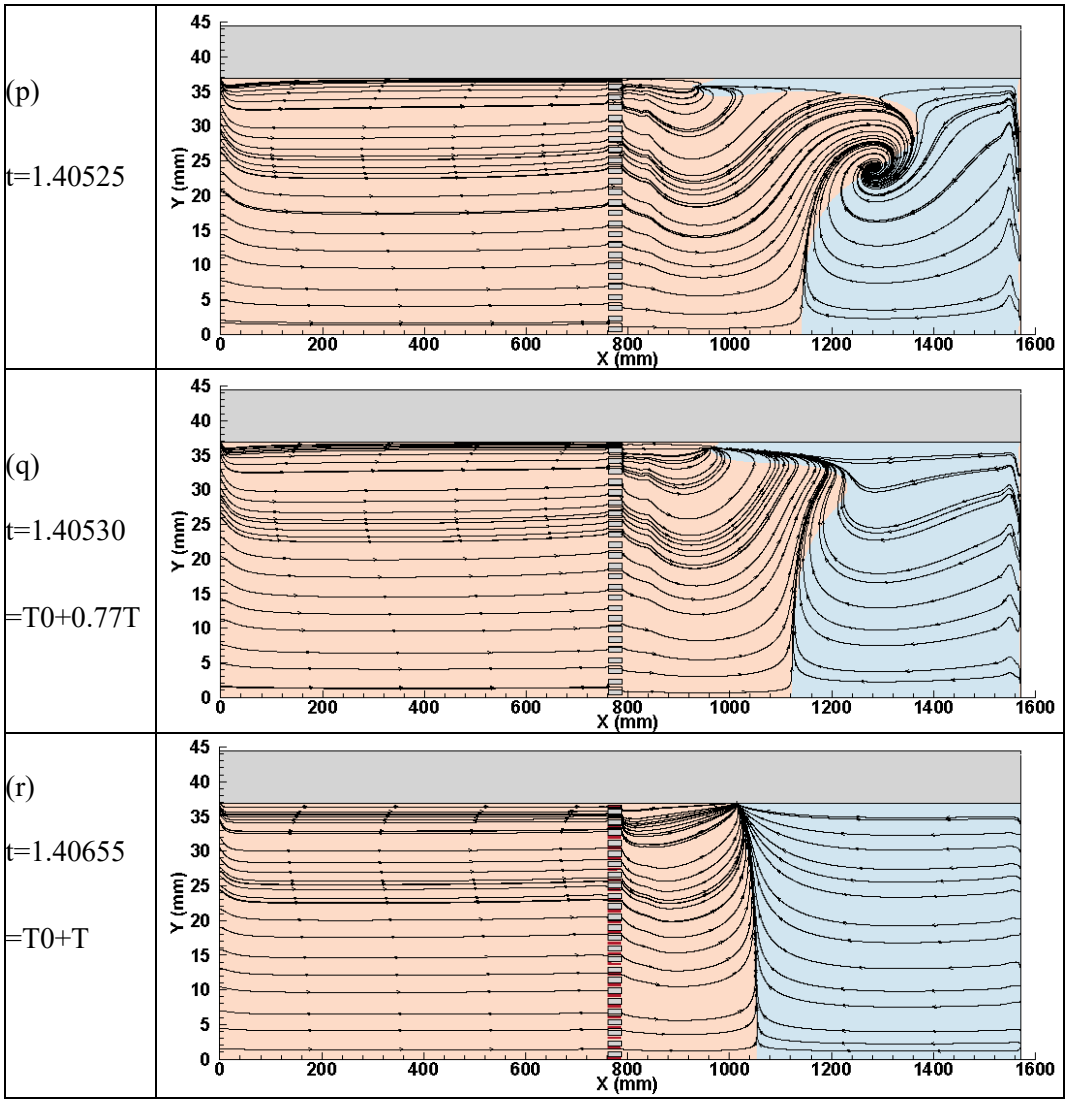

Figure 3-17. Axis velocity distribution in a cycle.

Figure 3-18 and Figure 3-19 show the temperature distribution and kinetic rate of the reaction at time T0+T/4 in Figure 3-15, which represent the velocity fluctuation varying from positive to negative, and the time T0+3T/4 in Figure 3-15, which represent the transient the velocity fluctuation varying from negative to positive, respectively. It can be seen that the distance between the flame and the flame stabilizer outlet is far in Figure 3-18 (a) and Figure 3-19 (a) but close in Figure 3-18 (b) and Figure 3-19 (b).

In Figure 3-17, we have analyzed that, after the transient T0+T/4, the flow velocity in the flame zone changes direction to the backward direction. Thus, this is the furthest distance between the flame stabilizer to the flame. After this second, the flame will move to the upstream direction pushed by the negative flow. Until time T0+T/4, the

flame reaches its most left location, then the flow in the flame zone changes direction to the forward direction, with the flame then moving to the downstream direction.

In Figure 3-18 (a) and Figure 3-19 (a), as time proceeds, the positive flow velocity moves the flame downstream, as shown in Figure 3-17 (e), and the flow before the 2/3 tube length is compressed to the maximum limit. Then, the pair of vortices break down, and the flow is reversed, as shown in Figure 3-17 (f), where a vortex forms and the flow velocity decreases with time, causing the flow to become negative. The negative flow pushes the flame in the upstream direction, reaching the nearest point shown in Figure 3-18 (b) and Figure 3-19 (b), at which time the flow in the left tube is compressed to the maximum limit, new separation points are generated, and new vortices change the flow direction again, making the flame surface move downstream.

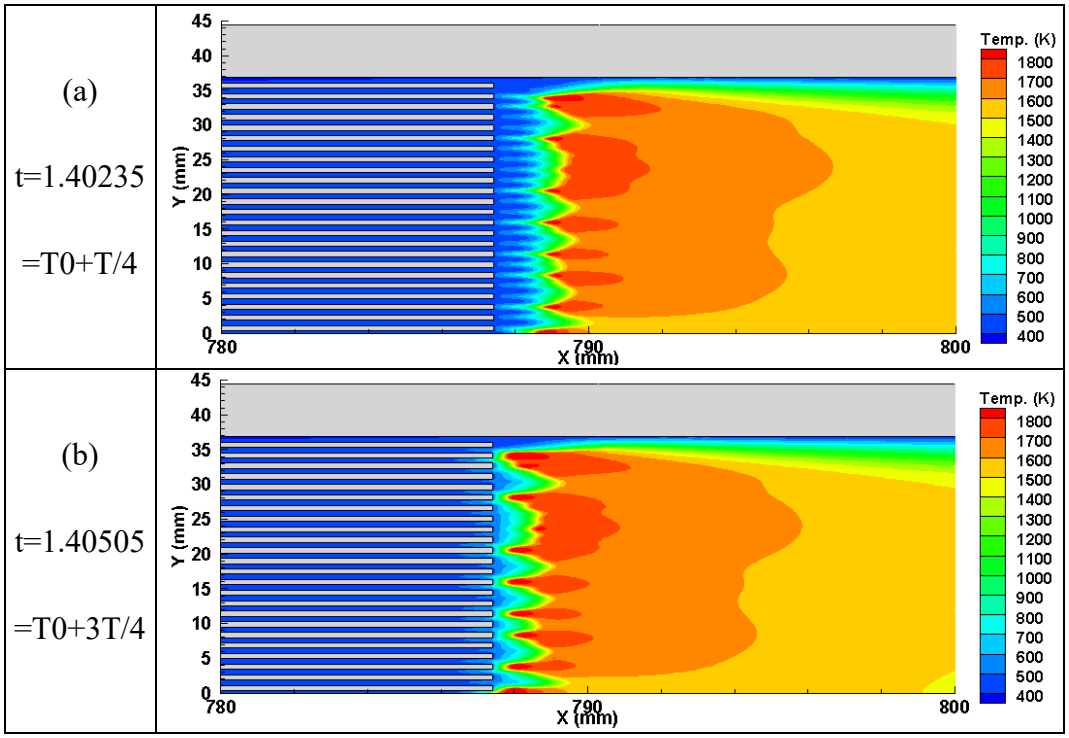

Figure 3-18. Temperature distribution at different times.

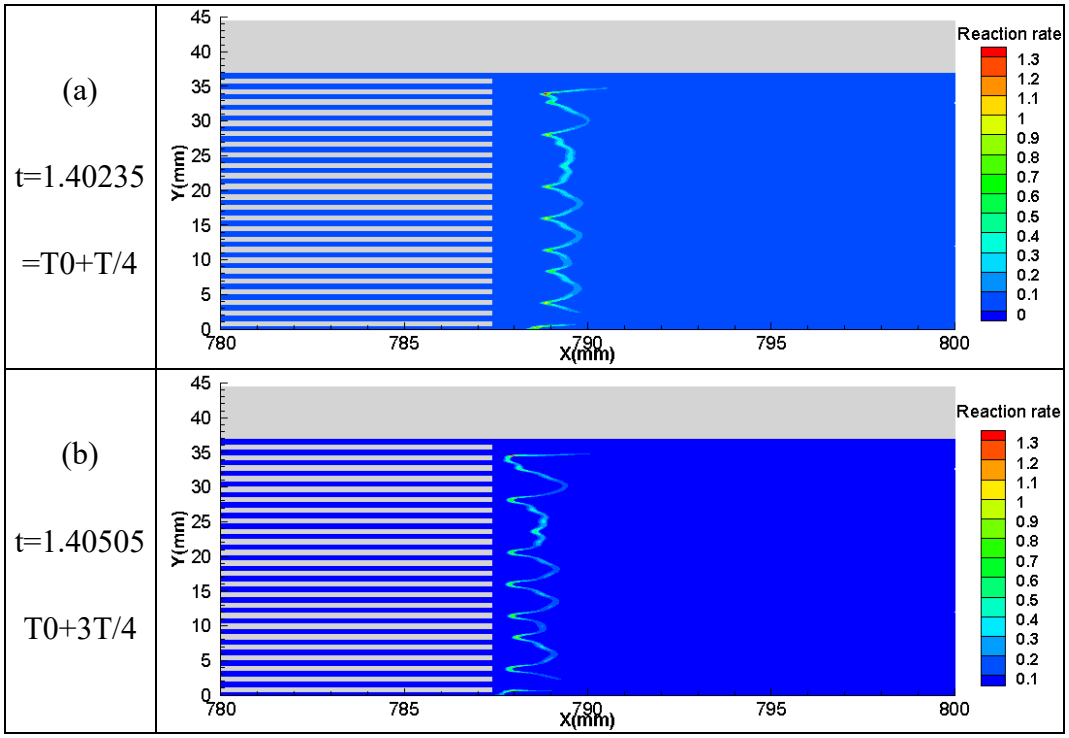

Figure 3-19. Kinetic rate of reaction at different times.

Thus, it can be concluded that the distance between the flame and flame stabilizer varies with the change in the axial velocity in the limit cycle state, the flow between the flame stabilizer and the 2/3 tube length is compressed when the axial velocity is positive, while it is expanded when the axial velocity is negative. During this periodic compression and expansion, the streamline is stretched and distorted, leading to the periodic formation and disappearance of vortices in the tube. This periodic behavior of the velocity field influences both the shape and distance of the flame via feedback; since the oscillation of pressure and heat release are in phase, this forward feedback is encouraged. The amplitudes of these oscillations increasing exponentially until they reach a balance that the energy released into the system and the losses are equation in one cycle, then the oscillation will maintain at that amplitudes, resulting in limit cycle thermoacoustic oscillations.

3.5. Conclusions

A two-dimensional CFD simulation of the combustion stability in a Rijke burner is conducted in this work. The self-excited thermoacoustic instability is numerically

captured and analyzed, and the following conclusions are drawn.

1) The onset and growth of the thermoacoustic instability are successfully captured. The simulated growth of the instability G is 1.22×10^{-2} $\mathrm{rad/s^2}$, which is less than the maximum possible growth rate because of the acoustic loss and boundary loss.

2) In the limit cycle oscillation state, the velocity has a 88.1° phase advance relative to the pressure, the reaction heat release has a 24.3° phase delay relative to the pressure, which fulfills the Rayleigh Criterion that oscillations are encouraged when heat fluctuates in phase with pressure perturbation. The reaction heat has a 114.34° phase delay relative to the velocity. This time delay is a critical factor that induces combustion instability in the Rijke tube system.

3) The simulated oscillation frequency and mode are in good agreement with the 1-D analytical results. The simulated pressure oscillation frequency is 6% higher than the analytical results based on the inlet parameters since the reaction heat increases the flow temperature and the sound speed. The normalized pressure and normalized velocity along the centerline are in agreement with the prediction results of the second acoustic mode.

4) As the system is excited into a limit cycle oscillation state, the amplitude of the velocity perturbation is larger than the average steady-state flow; thus, in some local areas, the flow velocity may be below zero, resulting in local backward flow in the burner. The forth and back flow in the flame zone push the flame surface moving downstream and upstream, causing unwanted flame flashback or even flameout.

5) In the limit cycle state, the distance between the flame and honeycomb outlet varies with the periodic change in the axial velocity. The flow between the flame stabilizer and the 2/3 tube length is periodically compressed and expanded, while the streamline is periodically stretched and distorted, inducing the periodic formation and disappearance of vortices in the tube. This is typical behavior of flame-induced

vortices, which leads to the flow field transition from laminar flow to turbulent flow.

6) The periodic behavior of the flow field induced by the unsteady heat release influences both the shape and distance of the flame via feedback; thus, the forward interaction between the heat release and flow perturbation results in thermoacoustic instability.

4. Conclusions and future work

Nonlinear analysis and CFD simulation of combustion instability are performed in this work. A new saturated flame model is proposed and the bifurcation characteristic of a 1D Rijke tube burner is performed based on the new flame model. The dynamic flow field in a Rijke burner is simulated to investigate the dynamic flow field when combustion instability happens.

4.1. The main work and conclusions

The main contents of this work are as follows:

1) The acoustic perturbation equation of the 1D Rijke burner is derived and projected to a finite-dimensional function space which is constituted by the natural acoustic modes of the burner. A saturated flame model is proposed and applied in the analysis of this work. A Matlab procedure is programmed to solve the governing equation and analyze the combustion instability from the view of nonlinear dynamics.

2) The stabilities of the system under given conditions are determined by calculating the eigenvalues. Then the bifurcation analysis of the dynamics behavior for the Rijke burner is performed for the variation of flame location. Subcritical bifurcation occurs, and the bistable region appears when keep varying the flame location, behaving as the hysterical phenomena when varying the flame location from different directions of the tube.

3) The bifurcation analysis of the dynamics behavior for the Rijke burner is performed for the flame heat release intensity. Supercritical bifurcation occurs, implying that there is no bistable regime when varying the flame heat release intensity under this flame model. Besides, both the unstable area and the oscillation amplitude of the system increase with the increase of the flame heat release intensity since more heat energy is converted into sound energy.

4) The bifurcation analysis of the dynamics behavior for the Rijke burner is performed

for the time lag between heat release and flow velocity perturbation. The system stability switches between stability and instability as the time delay increases under given flame location and flame intensity. This is called stability switching and is a typical nonlinear phenomenon in a delay-dependent system.

5) The time evolution of the pressure and velocity oscillations are analysis by the Phase diagram and Poincaré map, and the exponential growth rate of the system in the oscillating stage and the decay stage are given.

6) A two-dimensional CFD simulation of a Rijke burner is conducted. The self-excited thermoacoustic instability is numerically simulated. The onset and growth of the thermoacoustic instability are successfully captured. The simulated growth rate of the instability is 1.22×10^{-2} $\mathrm{rad/s^2}$, Which is less than the maximum possible growth rate, implying the damping effect of boundary layer and acoustic loss.

7) The simulated oscillation frequency and mode of the oscillation are in good agreement with the 1-D analytical results. The pressure and velocity along the centerline are in agreement with the prediction results.

8) The velocity perturbation amplitude is larger than the average steady-state flow at the limit cycle oscillation state, meaning there is unwanted backward flow in the burner.

9) The flow between the flame stabilizer and the node section is periodically compressed and expanded, while the streamline is periodically stretched and pressed, inducing the periodic formation and disappearance of vortices in the tube. While in one cycle, the flow is laminar most of the time, and the vortices appear to change the velocity distribution of the flow field in a short time.

10) The periodic behavior of the flow field induced by the unsteady heat release influences both the shape and distance of the flame via feedback; thus, the forward interaction between the heat release and flow perturbation results in thermoacoustic instability.

4.2. Innovations

The innovations of this research are shown in:

1) A saturated flame model is proposed to reasonably describe the flame's unsteady heat release for velocity amplitudes that are greater than the mean velocity, e.g., where reversal flow occurs at the flame area. With the new saturated flame model, the nonlinear behaviors of combustion instabilities are studied.

2) The dynamic of the flow field of combustion instability is captured by CFD simulation, the onset and exponential increase of pressure oscillation are calculated, the large-scale streamline roll-up is founded when the flow changes direction.

4.3. Future work

1) The current work is based on a 1D analytical work and 2D CFD modeling work. 2D analysis can predict the structure of the combustion field in the Rijke burner under low Reynold number conditions with the asymmetric assumption. However, 3D simulation can get information on the circumferential direction, which should not be ignored in more complicated cases. For the subsequent work, a 3D simulation should be attempted to study the actual non asymmetric combustion field.

2) With the development of high-performance computers, Direction Numerical Simulation (DNS), which solves the instantaneous Navier–Stokes equations without any simplified model, becomes possible. DNS would predict all turbulence scales and their effects on combustion like a high-resolution sensor would measure them in an experiment. For the combustion insatiability problems involving coupling of fluid mechanisms, complicated reactions, and heat and mass transfer process, DNS would be a powerful tool to simulate the detail with high precise details in the research of combustion instability. Thus, to used the DNS method to get more credible information would have great value in the research of combustion instability.

References

[1] Juniper M P, Sujith R I. Sensitivity and nonlinearity of thermoacoustic oscillations. Annual Review of Fluid Mechanics,2018,50(1):661-689.

[2] Gotoda H, Nikimoto H, Miyano T, Tachibana S. Dynamic properties of combustion instability in a lean premixed gas-turbine combustor. Chaos,2011,21:013124.

[3] Rijke P L, Notiz üoti eine neue Art, die in einer an beiden Enden offenen Röhre enthaltene Luft in Schwingungen zu versetzen. Ann. Phys.,1859,183(6):339-343.

[4] Ruan R L, Beckstead M W, Finlinson J C, et al. A review of Rijke tubes, Rijke burners and related devices. Prog. Energy Combust. Sci. 1993,19:313-364.

[5] Sarpotdar S M, Ananthkrishnan N, Sharma S D. The Rijke tube — A thermo-acoustic device. Reson., 2003, 8, 59–71.

[6] Kabiraj L, Sujith R I, Wahi P. Bifurcations of self-excited ducted laminar premixed flames. J. Eng. Gas Turbines Power, 2011,134,031502.

[7] Zhao D, Chow Z. Thermoacoustic instability of a laminar premixed flame in Rijke tube with a hydrodynamic region. J. Sound Vib.,2013,332,3419-3437.

[8] Weng F, Zhu M, Jing L. Beat: A nonlinear thermoacoustic instability in Rijke burners. Int. J. Spray Combust. Dyn.,2014,6,247-266.

[9] Weng F, Li S, Zhong D, Zhu M. Investigation of self-sustained beating oscillations in a Rijke burner. Combust. Flame,2016,166,181-191.

[10] Fleifil M. Response of a laminar premixed flame to flow oscillations: A kinematic model and thermoacoustic instability results. Combust. Flame,1996,106,487-510.

[11] Dowling A P. A kinematic model of a ducted flame. J. Fluid Mech.,1999,394, 51-72.

[12] Dowling, A.P. Nonlinear self-excited oscillations of a ducted flame. J. Fluid Mech., 1997,346,271-290.

[13] Zinn B T. A theoretical study of nonlinear combustion instability in liquid-propellant rocket engines. AIAA J.,1968,6, 1966-1972.

[14] Zinn B T, Lores M E. Application of the Galerkin method in the solution of nonlinear axial combustion instability problems in liquid rockets. Combust. Sci. Technol.,1971,4,269-278.

[15] Lord Rayleigh. The Theory of Sound, Vol. II; Dover: New York, NY, USA, 1945.

[16] Culick F. Some recent results for nonlinear acoustics in combustion chambers. AIAA J.,1994,32,146-169.

[17] Culick F. Nonlinear behavior of acoustic waves in combustion chambers—I. Acta Astronaut.,1976,3,715-734.

[18] Culick F. Nonlinear behavior of acoustic waves in combustion chambers—II. Acta Astronaut.,1976,3,735-757.

[19] Culick F, Burnley V, Swenson G. Pulsed instabilities in solid-propellant rockets. J. Propuls. Power.,1995,11,657-665.

[20] Balasubramanian K, Sujith R I. Non-normality and nonlinearity in combustion–acoustic interaction in diffusion flames. J. Fluid Mech.,2007,594,29-57.

[21] Yoon H G, Peddieson J, Purdy K R. Mathematical modeling of a generalized Rijke tube. Int. J. Eng. Sci.,1998,36,1235-1264.

[22] Yoon H G, Peddieson J, Purdy K R. Nonlinear response of a generalized Rijke tube. Int. J. Eng. Sci.,2001,39,1707-1723.

[23] Li XY, Huang Y, Zhao D, Yang W, et al. Stability study of a nonlinear thermoacoustic combustor: Effects of time delay, acoustic loss and combustion-flow interaction index. Appl. Energy, 2017,199,217-224.

[24] Wang QZ. Computational investigations of boundary condition effects on simulations of thermoacoustic instabilities. Ph.D. Thesis, Virginia Polytechnic Institute and State University, Blacksburg, VA, USA, 2015.

[25] Chatterjee P, Vandsburger U, Saunders W R, et al. On the spectral characteristics of a self-excited Rijke tube combustor—numerical simulation and experimental measurements. J. Sound Vib.,2005,283,573-588.

[26] Chatterjee K, Kumar A, Chatterjee S, et al. Numerical simulation to characterize homogeneity of air-fuel mixture for premixed combustion in gas turbine combustor. In Proceedings of the ASME 2012 Gas Turbine India Conference, Mumbai, India, 1 December 2012,461-468.

[27] Blanchard R, Ng W, Lowe K T T, et al. Simulating bluff-Body flameholders: on the use of proper orthogonal decomposition for wake dynamics validation. J. Eng. Gas Turbines Power,2014,136,122603.

[28] Ghulam M M, Gutmark E J. Computational aeroacoustics for analyzing thermo-acoustic instabilities in afterburner ducts. In proceedings of the 2018 Joint Propulsion Conference, Cincinnati, OH, USA, 9–11 July 2018.

[29] Zhao D, Gutmark E, De Goey, P. A review of cavity-based trapped vortex, ultra-compact, high-g, inter-turbine combustors. Prog. Energy Combust. Sci.,2018,66,42-82.

[30] Rott N. Thermoacoustic. Advances in Applied Mechanics.1980,20,135-175.

[31] Rott N. Damped and thermally driven acoustic oscillations in wide and narrow tubes. Journal of Applied Mathematics and Physics.,1969,20.

[32] Rott N. Thermally driven acoustic oscillations. part II: stability limit for helium. Journal of Applied Mathematics and Physics,1973,24.

[33] Rott N. Thermally driven acoustic oscillations, part III: second-order heat flux. Journal of Applied Mathematics and Physics,1975,26.

[34] Rott N. The influence of heat conduction on acoustic streaming. Journal of Applied Mathematics and Physics,1974, 25.

[35] Mfiller U A, Rott N. Thermally driven acoustic oscillations, part VI: excitation and power. Journal of Applied Mathematics and Physics,1983, 34.

[36] Heckl M A. Non-linear acoustic effects in the Rijke tube. Acustica,1990,72,63-71.

[37] Han F, Sha JZ. Study on nonlinear increasing procedure of Rijke thermoacoustic instability. Acta Acustica,1996,21,362-367. (in Chinese)

[38] Han F, Yue GS, Sha JZ. Nonlinear effect of Rijke thermoacoustic oscillation. Acta Acustica,1997,22,249-254. (in Chinese)

[39] Matveev K I. Thermoacoustic instability in the Rijke tube: experimental and modeling. California: California Institute of Technology,2003, Ph. D. Dissertation.

[40] Balasubramanian K, Sujith R I. Thermoacoustic instability in a Rijke tube: Non-normality and nonlinearity. 2008 Phys. Fluids,2008,20,044103.

[41] Subramanian P, Mariappan S, Sujith R I, et al. Bifurcation analysis of

thermoacoustic instability in a horizontal Rijke tube. Int. J. Spray Combust. Dyn.,2010,2(4),325-355.

[42] Ma DY. Fundamental Theory of Modern Acoustic1. Beijing: Science Press,2004,321-363. (in Chinese)

[43] Li GN, Zhou H, Li SY. et al. frequency hopping of thermoacoustic instability in Rijke-type combustor. J. Eng. Therm.,2008,29,879-892. (in Chinese)

[44] Huang X, Hu ZJ, Li Q, et al. Advances in research of mechanism of Rijke-type thermoacoustic self-excited oscillation. Cryogenics,2010,173(1),5-10. (in Chinese)

[45] Sayadi T, Chenadec V L, Schmid P J, et al. Massot Thermoacoustic instability – a dynamical system and time domain analysis. J. Fluid Mech., 2014,753,448-471.

[46] Kashinath K, Waugh I C, Juniper M P. Nonlinear self-excited thermoacoustic oscillations of a ducted premixed flame: bifurcations and routes to chaos. J. Fluid Mech., 2014,761,399-430.

[47] Howe M S. Acoustics of Fluid-Structure Interactions. Cambridge: Cambridge University Press,1998,469-472.

[48] Subramanian P, Sujith R I, Wahi P. Subcritical bifurcation and bistability in thermoacoustic systems. J. Fluid Mech.,2013,715,210-238.

[49] Juniper M P. Triggering in the horizontal Rijke tube: non-normality, transient growth and bypass transition. J. Fluid Mech.,2011,667,272-308.

[50] Moeck, J. P., Bothien, M. R., Schimek, S., et al.: Subcritical thermoacoustic instabilities in a premixed combustor. 14th AIAA/CEAS Aeroacoustics Conference (29th AIAA Aeroacoustics Conference) Vancouver, British Columbia, Canada,2008.

[51] Bellow B D, Bobba M K, Forte A, et. al. Flame transfer function saturation mechanisms in a swirl-stabilized combustor. Proceedings of the Combustion Institute,2007, 31, 3181-3188.

[52] Ananthkrishnan, N., Deo, S., Culick, F. E. C.: Reduced-order modeling and dynamics of nonlinear acoustic waves in a combustion chamber. Combust. Sci. Technol. 2005,177(2), 221-247.

[53] Wang, Z., Liu P., Ao W.: A reduced-order model of thermoacoustic instability in solid rocket motors. Aerosp. Sci. Technol.2020, 97, 105615.

[54] Frankel, M. L., Kovačič, G., Roytburd, V., et al.: Finite-dimensional dynamical system modeling thermal instabilities. Phys. D: Nonlinear Phenom. 2000,137 (3–4), 295–315.

[55] Sieber, J., Engelborghs, K., Luzyanina, T., et al.: DDE-BIFTOOL v. 3.0 Manual—Bifurcation Analysis of Delay Differential Equations. 2014.

[56] Engelborghs, K., Luzyanina, T., Roose, D., et al.: Numerical bifurcation analysis of delay differential equations using DDE-BIFTOOL. ACM Transactions on Mathematical Software 2002,28, 1–2.

[57] Huang Y, Yang V: Dynamics and stability of lean-premixed swirl-stabilized combustion. Prog. Energy Combust. Sci. 2009, 35(4), 293-364.

[58] Li J , Xia Y, Morgans A S , et al.: Numerical prediction of combustion instability limit cycle oscillations for a combustor with a long flame. Combust. Flame,2017, 185, 28-43.

[59] Ananthkrishnan N, Deo S, Culick F E C.: Reduced-order modeling and dynamics of nonlinear acoustic waves in a combustion chamber. Combust. Sci. Technol.2005,

177(2), 221-247

[60] Cao S, Zhang J, Deguchi Y, et al.: Analysis of mass transport in a turbulent flame using Lagrangian coherent structures. Journal of vibration testing and system dynamics, 2020 4(1), 79-93.

[61] Lieuwen, T.C.: Unsteady combustor physics. Cambridge university press. Cambridge, 2012.

[62] Zhao D, Guan Y, Arne R. Characterizing hydrogen-fuelled pulsating combustion on thermodynamic properties of a combustor. Commun. Phys.,2019,2,44.

[63] Li Z, Zhang H. Numerical simulations of one-dimensional laminar premixed CH4/air flames using the detailed and one-step reaction mechanisms. J. Tsinghua. Univ. (Sci. & Tech.),2015,45(11),1510-1512.

[64] Acampora L, Marra F S, Martelli E. Comparison of different CH4-Air combustion mechanisms in a perfectly stirred reactor with oscillating residence times close to extinction. Combust. Sci. Technol.,2016,188 (4-5),707-718.

[65] Westbrook C K, Dryer F L. Chemical kinetic modeling of hydrocarbon combustion. Prog. Energy Combust. Sci.,984,10,1-57.

[66] Turns S R. An introduction to combustion: concepts and applications. The McGraw-Hill Companies, Inc.: Singapore, 2000.

[67] Abbud-Madrid A, Ronney P D. Effects of radiative and diffusive transport processes on premixed flames near flammability limits. Symp. Int. Combust.,1991,23,423-431.

[68] Howell J R, Pinar M, Siegel R. Thermal radiation heat transfer. CRC Press: Boca

Raton, FL, USA, 2015.

[69] Ratzel A C, Howell J R. Two-dimensional radiation in absorbing-emitting media using the P-N approximation. J. Heat Transf.,1983,105,333-340.

[70] Cheng P. Two-dimensional radiating gas flow by a moment method. AIAA J.,1964,2, 1662-1664.

[71] Sazhin S, Sazhina E., Faltsi-Saravelou, O, et al. The P-1 model for thermal radiation transfer: Advantages and limitations. Fuel,1996,75,289-294.

[72] Krishnamoorthy G. A computationally efficient P1 radiation model for modern combustion systems utilizing pre-conditioned conjugate gradient methods. Appl. Therm. Eng.,2017,119,197-206.

[73] Karyeyen S. Combustion characteristics of a non-premixed methane flame in a generated burner under distributed combustion conditions: A numerical study. Fuel, 2018,230,163-171.

[74] Kana-Donfack P, Kapseu C, Tcheukam-Toko D, et al. Numerical modeling of sugarcane bagasse combustion in sugar mill boiler. J. Energy Power Eng.,2019,13, 80-90.

[75] Zhang Y, Wang C, Liu X, et al. Numerical study of the self-excited thermoacoustic vibrations occurring in combustion system. Appl. Therm. Eng.,2019,160,113994.

[76] Zhao D. Thermodynamics-acoustics coupling studies on self-excited combustion oscillations maximum growth rate. J. Therm. Sci.,2020,1-13.

Acknowledgments

I would like to thank all of you for your help in writing this paper.

My deep gratitude is first to my supervisor, Yoshihiro Deguchi, my supervisor, for his valuable encouragement and guidance. Thanks to his extraordinary suggestion and support, I accomplished the thesis.

Secondly, I would like to express my sincere thanks to Professor Zhang Jiazhong and Professor Wang Zhenzhen at Xi'an Jiaotong University for they give me the chance to apply for the Double Degree Program of Tokushima University.

I wish to thank Cao Shengli, Wang Wei, Wang Qiming, Ms. Muramoto, and all the members of our laboratory, who have given me their kind help during the period I studied in Tokushima; I am also very grateful to Ms. Asada and her colleagues for their help of me in living in Tokushima. With the help of them, I have a great time in Japan.

Finally, I would like to thank my dear family for their love and great support, offering me resources and encouragement during the years of study.